

# The *R*-Process Alliance: Detailed Chemical Composition of an *R*-Process Enhanced Star with UV and Optical Spectroscopy

Shivani P. Shah,<sup>1\*</sup> Rana Ezzeddine,<sup>1</sup> Ian U. Roederer,<sup>2,3,4</sup> Terese T. Hansen,<sup>5</sup> Vinicius M. Placco,<sup>6</sup> Timothy C. Beers,<sup>7,4</sup> Anna Frebel,<sup>8,4</sup> Alexander P. Ji,<sup>9,10</sup> Erika M. Holmbeck,<sup>11</sup> Jennifer Marshall,<sup>12</sup> Charli M. Sakari<sup>13</sup>

<sup>1</sup>*Department of Astronomy, University of Florida, 211 Bryant Space Science Center, Gainesville, FL 32601, USA*

<sup>2</sup>*Department of Physics, North Carolina State University, Raleigh, NC 27695, USA*

<sup>3</sup>*Department of Astronomy, University of Michigan, Ann Arbor, MI 48109, USA*

<sup>4</sup>*Joint Institute for Nuclear Astrophysics – Center for the Evolution of the Elements (JINA-CEE), USA*

<sup>5</sup>*Department of Astronomy, Stockholm University, AlbaNova University Centre, SE-106 91 Stockholm, Sweden*

<sup>6</sup>*NSF’s NOIRLab, Tucson, AZ 85719, USA*

<sup>7</sup>*Department of Physics and Astronomy, University of Notre Dame, Notre Dame, IN 46556, USA*

<sup>8</sup>*Department of Physics and Kavli Institute for Astrophysics and Space Research, Massachusetts Institute of Technology, Cambridge, MA 02139, USA*

<sup>9</sup>*Department of Astronomy & Astrophysics, University of Chicago, 5640 S Ellis Avenue, Chicago IL 60637, USA*

<sup>10</sup>*Kavli Institute for Cosmological Physics, University of Chicago, Chicago IL 60637, USA*

<sup>11</sup>*The Observatories of the Carnegie Institution for Science, 813 Santa Barbara St, Pasadena, CA 91101, USA*

<sup>12</sup>*Mitchell Institute for Fundamental Physics and Astronomy and Department of Physics and Astronomy, Texas A&M University, College Station, TX 77843-4242, USA*

<sup>13</sup>*Department of Physics & Astronomy, San Francisco State University, San Francisco CA 94132, USA*

Accepted 2024 January 16. Received 2024 January 14; in original form 2023 December 19

## ABSTRACT

We present a detailed chemical-abundance analysis of a highly *r*-process-enhanced (RPE) star, 2MASS J00512646-1053170, using high-resolution spectroscopic observations with *Hubble Space Telescope*/STIS in the UV and Magellan/MIKE in the optical. We determined abundances for 41 elements in total, including 23 *r*-process elements and rarely probed species such as Al II, Ge I, Mo II, Cd I, Os II, Pt I, and Au I. We find that  $[\text{Ge}/\text{Fe}] = +0.10$ , which is an unusually high Ge enhancement for such a metal-poor star and indicates contribution from a production mechanism decoupled from that of Fe. We also find that this star has the highest Cd abundance observed for a metal-poor star to date. We find that the dispersion in the Cd abundances of metal-poor stars can be explained by the correlation of Cd I abundances with the stellar parameters of the stars, indicating the presence of NLTE effects. We also report that this star is now only the 6th star with Au abundance determined. This result, along with abundances of Pt and Os, uphold the case for the extension of the universal *r*-process pattern to the third *r*-process peak and to Au. This study adds to the sparse but growing number of RPE stars with extensive chemical-abundance inventories and highlights the need for not only more abundance determinations of these rarely probed species, but also advances in theoretical NLTE and astrophysical studies to reliably understand the origin of *r*-process elements.

**Key words:** stars: abundances – stars: chemically peculiar – stars: Population II – ultraviolet: stars

## 1 INTRODUCTION

The rapid neutron-capture process (*r*-process) is thought to be responsible for synthesizing about half the isotopes of elements heavier than zinc (atomic number,  $Z > 30$ ) observed in the Solar System (S.S.) (Cameron 1957; Burbidge et al. 1957), with the slow neutron-capture process (*s*-process) responsible for synthesizing the other half. Easily detected *r*-process elements such as europium (Eu) have also been observed outside the S.S., in various Milky Way stars, stellar streams, and

dwarf galaxies (e.g., Venn et al. 2004; Ji et al. 2016; Delgado Mena et al. 2017; Marshall et al. 2019; Hansen et al. 2021; Ji et al. 2022, and references therein). However, the primary astrophysical site(s) of *r*-process nucleosynthesis is still unresolved, contributing to a substantial gap in our understanding of Galactic chemical enrichment and evolution (Cowan et al. 2021; National Academies of Sciences & Medicine 2021).

Theoretical studies investigating the properties of *r*-process astrophysical sites have typically relied on the S.S. *r*-process pattern to understand the range of *r*-process elements synthesized, and the relative quantities in which they are synthesized (e.g., Goriely & Arnould 2001; Schatz et al. 2002;

\* E-mail: shivani.shah@ufl.edu

Farouqi et al. 2010; Lippuner et al. 2017; Siegel et al. 2019; Curtis et al. 2023). However, the S.S.  $r$ -process pattern is not directly measured. Instead, it is obtained as the residual of the S.S.'s total chemical-abundance pattern after accounting for a theoretically derived  $s$ -process pattern (e.g., Arlandini et al. 1999; Sneden et al. 2008; Prantzos et al. 2020). In turn, the  $s$ -process pattern is obtained by calibrating stellar evolution and Galactic chemical-evolution models to the meteoritic abundance of  $s$ -process-only isotopes, with  $s$ -process abundances of all other isotopes theoretically inferred (Roederer et al. 2022a). Moreover, the S.S.  $r$ -process abundance pattern represents only a single  $r$ -process template, which is also the result of Galactic chemical evolution over billions of years.

On the other hand,  $r$ -process-enhanced (RPE) stars serve as more direct and reliable probe of  $r$ -process nucleosynthesis events, as well as provide the opportunity of obtaining many different  $r$ -process templates. RPE stars have  $r$ -process elemental abundances in excess of twice the Fe abundance as compared to the Sun,  $[\text{Eu}/\text{Fe}] > +0.3^1$  (Beers & Christlieb 2005; Holmbeck et al. 2020). RPE stars are typically very metal poor, with  $[\text{Fe}/\text{H}] \lesssim -2.0$ , and as a result, they have preserved the pristine chemical fingerprints of very few (in some cases just one) progenitor  $r$ -process nucleosynthesis events (Frebel 2018, and references therein). Additionally, the heavy-element abundance patterns of the RPE stars originate almost purely from the  $r$ -process, with minimal contributions from other processes, if any. Given all of this, RPE stars offer a unique view of  $r$ -process nucleosynthesis in the early Universe.

To fully leverage RPE stars, it is important to determine the abundances for a wide range of their  $r$ -process elements. Reliable abundances for the rare-earth  $r$ -process elements ( $55 < Z < 71$ ) can be obtained relatively easily via ground-based optical observations (e.g., Sneden et al. 2009; Gull et al. 2021). On the other hand, to reliably determine abundances for most of the other elements, including lighter elements at and between the first and second  $r$ -process peaks ( $30 < Z < 55$ ) and heavier elements at and around the third  $r$ -process peak ( $71 \lesssim Z < 84$ ), supplemental space-based ultraviolet (UV) observations are required (e.g., Siqueira Mello et al. 2013; Roederer et al. 2022a). In fact, robust abundance determinations for some of these elements, such as germanium (Ge,  $Z = 32$ ), selenium (Se,  $Z = 33$ ), cadmium (Cd,  $Z = 48$ ), tellurium (Te,  $Z = 52$ ), platinum (Pt,  $Z = 78$ ), and gold (Au,  $Z = 79$ ), have been possible solely because of UV observations by the *Hubble Space Telescope* (HST) (Cowan et al. 1996; Sneden et al. 1998; Cowan et al. 2002; Sneden et al. 2003; Roederer et al. 2010b, 2012b; Roederer & Lawler 2012a; Roederer et al. 2014b; Siqueira Mello et al. 2013).

UV observations of RPE stars are especially desired to characterize the signatures of a larger inventory of  $r$ -process elements. Signatures of the light  $r$ -process elements accessible via optical spectra (e.g., Sr, Y, Zr) have indicated that the abundances of these elements deviate from the "universal"  $r$ -process pattern observed for the rare-earth and third-peak elements (Sneden et al. 2000; Cowan et al. 2005; François et al. 2007; Siqueira Mello et al. 2014; Ji et al. 2016; Cowan et al. 2021, and references therein). The origin of these devia-

tions is still unknown, with different astrophysical sites, conditions, and processes being considered (e.g., Chiappini et al. 2011; Hansen et al. 2012; Wanajo 2013; Holmbeck et al. 2019; Roederer et al. 2022b; Roederer et al. 2023). However, the full extent of these deviations is still not even well-established for some elements, such as Se, Cd, and Te, due to their scarce abundances, which require high-resolution UV spectra (Roederer et al. 2022b). The abundances of these elements, especially at and around the second  $r$ -process peak are also crucial in constraining the effects of nuclear physical processes like fission cycling on the  $r$ -process abundances (Eichler et al. 2016; Vassh et al. 2019). Similarly, even though the heavier  $r$ -process elements exhibit a "universal" abundance pattern, elements such as Pt and Au at the third  $r$ -process peak have been observed in  $\sim 15$  and  $\sim 5$  RPE stars, respectively, questioning the extent of the  $r$ -process universality or alternatively holding undiscovered clues to the still unknown origin of the universality (although see Roederer et al. 2023).

UV observations also offer the opportunity to investigate NLTE effects for the neutral species of elements such as Mg, Al, Co, Ni, Mo, and Os. Specifically, they enable access to the dominant species (usually first ions) of these elements, while their minority species (neutral atoms) are accessible via optical observations (Roederer et al. 2010b; Peterson 2011; Roederer & Lawler 2021; Roederer et al. 2022a). A subsequent comparison between the abundances of the dominant and the minority species can promote an empirical assessment of the theoretically predicted NLTE effects for the minority species of the elements, and thereby an assessment of the NLTE models themselves.

However, there are only a few RPE stars that have been analyzed with space-based UV observations and ground-based optical observations. These include HD 222925 (Roederer et al. 2018, 2022a), CS 31082-001 (Cayrel et al. 2001; Hill et al. 2002; Plez et al. 2004; Barbuy et al. 2011; Siqueira Mello et al. 2013), CS 22892-052 (Sneden et al. 2003), HD 108317 (Roederer et al. 2012a, 2014a,b), BD +17 3248 (Cowan et al. 2002; Roederer et al. 2010b), HD 160617 (Roederer & Lawler 2012b; Peterson et al. 2020), HD 84937 (Peterson et al. 2020), and HD 19445 (Peterson et al. 2020). The scarcity of such studies partly arises from the need of an RPE star to be bright in the NUV (e.g., GALEX  $NUV < 15$ ) in order to achieve the necessary signal-to-noise ratio (e.g., Roederer et al. 2022b). Additionally, since the strength of the absorption lines are decreased in such NUV-bright stars due to their higher effective temperatures, the stars also have to be sufficiently  $r$ -process enhanced to obtain abundances for a wide range of  $r$ -process elements. Studies of these stars have typically resulted in the determination of  $\sim 25$  to  $35$   $r$ -process elemental abundances for these stars. An exception to this case is HD 222925, for which abundances of a record 42  $r$ -process elements were determined. While these studies have already resulted in important theoretical implications for  $r$ -process-nucleosynthesis (e.g., Roederer et al. 2022b; Holmbeck et al. 2023), further advances in the field are still limited by the small number of stars that are studied in this manner.

In this paper, we present a detailed chemical-abundance analysis of a highly  $r$ -process-enhanced star, 2MASS J00512646-1053170 (hereafter J0051-1053), using UV observations with the *Space Telescope Imaging Spectrograph* (STIS) on board HST and optical observations with the *Magellan Inamori Kyocera Echelle* (MIKE) instrument at the

<sup>1</sup>  $[A/B] = \log(N_A/N_B)_{\text{Star}} - \log(N_A/N_B)_{\text{Solar}}$ , where  $N$  is the number density of the element.

Magellan II telescope. This star is unique from most other RPE stars studied with UV and optical spectroscopy, since it is possibly the warmest star in the sample ( $\sim 6400$  K) which is also highly  $r$ -process enhanced ( $[\text{Eu}/\text{Fe}] \sim +1.30$ ) and very low in metallicity ( $[\text{Fe}/\text{H}] \sim -2.30$ ).

This paper is organized as follows: In Section 2, we provide a brief overview of the discovery and previous literature studies of J0051-1053. In Section 3, we describe the data collection and reduction. Stellar parameter determination is outlined in Section 4, while the linelist and atomic data used are specified in Section 5. We describe the abundance determination of all the elements in Section 6. We detail the detection threshold method in Section 7, and the uncertainty analysis in Section 8. We discuss the results in Section 9, and conclude in Section 10.

## 2 PEDIGREE OF J0051-1053 AND ITS POSSIBLE HELMI STREAM MEMBERSHIP

J0051-1053 was first identified as a candidate metal-poor star by the Hamburg/ESO Survey, and then confirmed to have  $[\text{Fe}/\text{H}] = -2.43$  through medium-resolution ( $R \sim 2000$ ) spectroscopic followup with the 4 m Blanco telescope at the Cerro Tololo Inter-American Observatory (Frebel et al. 2006). Subsequently, J0051-1053 was identified as a possible member of the Helmi Stream by Beers et al. (2017). J0051-1053 was then identified by Ezzeddine et al. (2020) as a highly  $r$ -process-enhanced star with  $[\text{Eu}/\text{Fe}] = 1.34$  through higher-resolution spectroscopy with Magellan/MIKE at the Las Campanas Observatory, Chile. Given the importance of its chemical properties as a possible Helmi stream member, J0051-1053 was studied in further detail by Gull et al. (2021), who obtained abundances for 12  $r$ -process elements.

We note that a more recent study by Koppelman et al. (2019), who identified  $\sim 600$  potential members of the Helmi stream using Gaia DR2 kinematic parameters of over 8 million stars, did not identify J0051-1053 as one of the members. A kinematic analysis of J0051-1053 by G. Limberg following the method in Limberg et al. (2021) with updated Gaia DR3 parameters also indicated that J0051-1053 is unlikely to be associated with the Helmi stream (private communication). Given this uncertainty, we do not discuss the membership of J0051-1053 further.

## 3 DATA ACQUISITION AND REDUCTION

### 3.1 Optical Data

We observed J0051-1053 on 2016 October 14 (MJD = 57675.15855) with Magellan/MIKE (Bernstein et al. 2003) at the Las Campanas Observatory for a total exposure time of 1200s, resulting in S/N of 150 per pixel at  $4000 \text{ \AA}$ . We used the  $0''.7$  slit with  $2 \times 2$  binning, which yielded a measured resolving power of  $R \sim 28,400/26,800$  in the blue and red arms, respectively. The blue- and red-arm spectra together cover a wavelength range of  $3350\text{--}9500 \text{ \AA}$ . We reduced the spectra of the star using CarPy (Kelson et al. 2000; Kelson 2003), and corrected the radial velocity by cross-correlating against a rest-frame Magellan/MIKE spectrum of G 64-12. We determined a resulting heliocentric radial velocity of  $56.91 \text{ km/s}$ .

To normalize the orders, we used SMHR<sup>2</sup>, specifically using a natural cubic spline function with sigma clipping and strong lines masked, which was followed by stitching the orders together to furnish the final spectrum.

### 3.2 Near-Ultraviolet Data

J0051-1053 was observed with HST/STIS (Kimble et al. 1998; Woodgate et al. 1998) on 2020 January 21, 22, and 23 (Hansen et al. 2019, Proposal ID: 15951). The star was observed with the E230M échelle grating centered at  $\lambda 2707 \text{ \AA}$ , providing a wavelength coverage from  $\sim 2275 - 3119 \text{ \AA}$ , and with the  $0''.2 \times 0''.2$  slit, providing  $R \sim 30,000$ <sup>3</sup>. The observations were made over 12 orbits (i.e., 12 continuous exposures), with 3 orbits in each visit. The total exposure time over the 12 orbits was  $\sim 5.65\text{h}$ , resulting in a S/N of 65 at  $2707 \text{ \AA}$ . The spectra were automatically reduced by the CALSTIS software package, and we downloaded the processed spectra from the Mikulski Archive for Space Telescopes. We corrected for the radial velocity of each exposure by cross-calibrating a synthetic spectrum of the star generated with MOOG (Snedden 1973). We normalized the orders using a natural cubic spline function with sigma clipping, and co-added the normalized orders of all the exposures before stitching to furnish the final spectrum<sup>4</sup>.

## 4 STELLAR PARAMETERS

We determined the effective temperature ( $T_{\text{eff}}$ ) and surface gravity ( $\log g$ ) of J0051-1053 photometrically, based on methods described in Roederer et al. (2018) and Placco et al. (2020). We preferred to use photometric determinations of  $T_{\text{eff}}$  and  $\log g$  since spectroscopic determinations based on LTE have been known to be inaccurate and requiring additional corrections (Thévenin & Idiart 1999; Frebel et al. 2013; Ezzeddine et al. 2017, 2020). Moreover, these methods follow the  $R$ -Process Alliance convention for homogeneity. We briefly describe the methods used below.

We determined  $T_{\text{eff}}$  using the color- $[\text{Fe}/\text{H}]-T_{\text{eff}}$  photometric relations of Casagrande et al. (2010), which require an estimate of the metallicity. We initially used  $[\text{Fe}/\text{H}] = -1.97$ , obtained with spectroscopic determination of the stellar parameters. With new  $T_{\text{eff}}$  and  $\log g$  estimates obtained photometrically, we re-determined  $[\text{Fe}/\text{H}]$  using equivalent-width (EW) measurements of Fe I lines in the optical. We repeated the  $T_{\text{eff}}$  and  $\log g$  calculation using the photometric relations with  $[\text{Fe}/\text{H}] = -2.33$ .

We calculated  $T_{\text{eff}}$  from the dereddened  $V - J$ ,  $V - H$ ,  $V - K$ , and  $J - K$  colors. We used the  $J$ ,  $H$ , and  $K$  magnitudes from 2MASS (Cutri et al. 2003, VizieR catalog II/246) and the Johnson  $V$  magnitude from DR9 of APASS (Henden & Munari 2014, VizieR catalog II/336). We adopted the reddening value,  $E(B - V)$ , of 0.001 from Schlafly & Finkbeiner (2011) for the line of sight of the star, with the  $A_{\lambda}$

<sup>2</sup> <https://github.com/eholmbeck/smhr-rpa/tree/py38-mp1313>

<sup>3</sup> <https://hst-docs.stsci.edu/stisihb/chapter-13-spectroscopic-reference-material/13-3-gratings/echelle-grating-e230m>

<sup>4</sup> <https://github.com/alexji/alexmods/blob/master/alexmods/specutils/continuum.py>

extinction coefficient for the color bands from [McCall \(2004\)](#). We chose to not use the  $B - V$  color, because the  $B$ -band is sensitive to the CH  $G$ -band in carbon-enhanced metal-poor stars, which was not taken into account in the photometric relations. However, as shown below, J0051-1053 was not found to be carbon enhanced. As described in [Roederer et al. \(2018\)](#), we then calculated  $T_{\text{eff}}$  for each color band by drawing the input parameters (magnitudes, reddening, and metallicity)  $10^4$  times from their corresponding error distributions, which we assumed to be Gaussian. We used the median value of the resulting  $T_{\text{eff}}$  distribution. For the final  $T_{\text{eff}}$ , we used the weighted average of  $T_{\text{eff}}$  from all the color bands. For the total uncertainty on  $T_{\text{eff}}$ , we used the uncertainty of the weighted average. As a result, we obtained  $T_{\text{eff}} = 6440 \pm 82$  K.

We calculated  $\log g$  using the following fundamental relation:

$$\log g = 4 \log T_{\text{eff}} + \log(M/M_{\odot}) - 10.61 + 0.4 \cdot (BC_V) + V - 5 \log(d) + 5 - 3.1 \cdot E(B - V) - M_{\text{bol},\odot} \quad (1)$$

For  $M$ , the mass of the star, we assumed  $0.8 \pm 0.08 M_{\odot}$ . For  $BC_V$ , the bolometric correction in the  $V$ -band, we used  $-0.22$  ([Casagrande & Vandenberg 2014](#)). We obtained the distance  $d = 3.11$  pc from [Bailer-Jones et al. \(2021\)](#).  $M_{\text{bol},\odot}$  is the Solar bolometric magnitude, equal to 4.75. We calculated the constant 10.61 from the Solar constants  $\log(T_{\text{eff}})_{\odot} = 3.7617$  and  $\log g_{\odot} = 4.438$ . We estimated  $\log g$  by drawing these input parameters  $10^4$  times from their error distribution and taking the median of the resulting distribution of  $\log g$ . For the uncertainty on  $\log g$ , we used the standard deviation of the distribution. We note that, in order to take the error distribution of  $T_{\text{eff}}$  into account as one of the inputs to the  $\log g$  calculation, we added 150 K in quadrature with the uncertainty calculated above (82 K) to account for other possible systematic uncertainties. This choice has a minimal impact on the  $\log g$  value. Finally, we obtained  $\log g = 4.02 \pm 0.07$  dex.

For determining  $\xi$  and  $[\text{Fe}/\text{H}]$ , we used the EWs of Fe I and Fe II lines, along with the  $T_{\text{eff}}$  and  $\log g$  values obtained above. For this, we used SMHR<sup>5</sup>, the next-generation spectroscopic analysis tool of SMH ([Casey 2014](#)). SMHR uses the radiative transfer code MOOG ([Snedden 1973](#)), which we used with the proper treatment of scattering included<sup>6</sup> ([Sobeck et al. 2011](#)). For the stellar model atmosphere, we employed the ATLAS9 1D plane parallel LTE grid ([Castelli & Kurucz 2003](#)) in SMHR. To determine  $\xi$ , we minimized the trend in the abundances of the optical Fe I lines and their reduced EWs. We obtained  $\xi = 1.59$  km/s. We assumed a fiducial uncertainty of 0.2 km/s on  $\xi$ . For  $[\text{Fe}/\text{H}]$ , we report the resulting mean abundance of the UV and optical Fe II lines, with  $T_{\text{eff}}$ ,  $\log g$ , and  $\xi$  fixed to the above values, which is  $[\text{Fe}/\text{H}] = -2.34$ . We assumed a fiducial uncertainty of 0.20 dex on  $[\text{Fe}/\text{H}]$  as well.

Given the  $T_{\text{eff}}$  and  $\log g$  of J0051-1053, and its position on the Hertzsprung-Russell diagram, we identify the star to be near the end of the turn-off phase and at the beginning of the subgiant phase. For the purpose of this paper, we refer to it as a turn-off star.

## 5 LINELIST AND ATOMIC DATA

We used `linemake`<sup>7</sup> ([Placco et al. 2021a,b](#)) to generate the linelists for the UV and optical absorption lines. We specifically used the updated parameters of the CH transitions from [Masseron et al. \(2014\)](#). The linelist included hyperfine splitting structure (HFS) for relevant transitions. Following [Roederer et al. \(2022a\)](#), we included the Au I line at 2376.28 Å, with oscillator strength ( $\log gf$ -value) from [Zhang et al. \(2018\)](#). We also updated the  $\log gf$ -values of Hf II lines and included additional Hf II lines from [Den Hartog et al. \(2021\)](#).

For abundance determination, we investigated absorption lines used by [Placco et al. \(2015\)](#), [Roederer et al. \(2018\)](#), [Ji et al. \(2020\)](#), and [Roederer et al. \(2022a\)](#). We also investigated additional absorption lines of light and heavy elements in the UV from the *National Institute of Standard and Technology Atomic Spectra Database* (NIST ASD) ([Kramida et al. 2022](#)). We present the final list of absorption lines used for abundance determination in Table A1, along with the corresponding atomic parameters of the lines. We used a total of 113 transitions in the UV and 402 transitions in the optical.

## 6 CHEMICAL ABUNDANCES

As described in Section 5, we used SMHR, along with MOOG and ATLAS9 stellar-atmosphere grid, for line-by-line spectral analysis and abundance determination. We determined abundances using EW measurements for Na I, K I, Ca I, Ti II, Fe I, Fe II, and Ni I lines in the optical. For all the other lines, we used spectral synthesis. We used the isotopic ratios of the  $r$ -process elements from [Snedden et al. \(2008\)](#).

For an overview, we present various results of the abundance analysis in tables. Table A1 lists, for all the absorption lines used, the atomic parameters (wavelength, excitation potential, and  $\log gf$ -value), the abundance determination technique used (EW or spectral synthesis), the resulting abundance, and the systematic uncertainty on the abundance. Table 1 lists the mean abundances of each species from the UV and optical spectra separately, along with the statistical uncertainty. Table 2 lists the adopted abundance for each element, along with the resulting  $[\text{X}/\text{Fe}]$  abundance ratio, the statistical uncertainty, the systematic uncertainty, and the total uncertainty.

In general, we adopted the abundance of the ionized species, if available. If unavailable, we adopted the NLTE-corrected abundance of the neutral species, if the NLTE correction grids were available in the literature. If neither of these cases applied, we adopted the LTE abundance of the neutral species. If available, we generally combined the UV and optical lines for abundance determination of each species by taking the average of all the lines. We further detail the abundance determination for all the elements below.

### 6.1 Li

We detected a strong Li I absorption feature at 6707.80 Å. We did not detect Li absorption at any other Li I transition lines (e.g., [Kowkabay et al. 2022](#)). We used spectral synthesis to fit the  $\lambda 6707$  line and determined  $\log \epsilon(\text{Li}) = 2.37$ . This

<sup>5</sup> <https://github.com/andycasey/smhr>

<sup>6</sup> <https://github.com/alexji/moog17scat>

<sup>7</sup> [https://github.com/vmplacco/linemake/tree/ch\\_masseron](https://github.com/vmplacco/linemake/tree/ch_masseron)

Species	$\log \epsilon(X)_{UV}$	$\sigma_{stat,UV}$	$N_{UV}$	$\log \epsilon(X)_{op}$	$\sigma_{stat,OP}$	$N_{OP}$	$\log \epsilon(X)$	$\Delta NLTE_{corr}$
LiI	–	–	–	2.37	0.20	1	2.37	–0.018
OI	–	–	–	7.08	0.05	3	7.08	–0.10
NaI	–	–	–	3.99	0.07	4	3.99	–0.10
MgI	5.66	0.04	2	5.73	0.09	7	5.72	0.10
MgII	5.70	0.20	1	–	–	–	5.70	–
AlI	–	–	–	3.32	0.17	2	3.32	0.47
AlII	4.18	0.20	1	–	–	–	4.18	–
SiI	5.58	0.20	1	5.53	0.20	1	5.56	0.003
SiII	5.60	0.01	2	5.47	0.20	1	5.55	–
SI	–	–	–	<5.98	–	5	<5.98	–
KI	–	–	–	3.33	0.20	1	3.33	–0.28
CaI	–	–	–	4.48	0.09	24	4.48	0.14
ScII	1.13	0.20	1	1.10	0.05	12	1.10	–
TiI	–	–	–	3.2	0.10	12	3.2	0.14
TiII	3.10	0.10	4	3.12	0.15	34	3.12	0.04
VI	–	–	–	2.05	0.2	1	2.05	–
VII	1.99	0.08	6	1.97	0.05	7	1.98	–
CrI	3.22	0.03	2	3.34	0.05	6	3.31	0.25
CrII	3.46	0.05	11	3.31	0.02	3	3.43	0.04
MnI	2.89	0.22	3	2.81	0.02	5	2.84	0.28
MnII	2.97	0.14	2	2.88	0.07	4	2.91	–0.025
FeI	5.16	0.11	21	5.19	0.1	156	5.19	0.17
FeII	5.10	0.12	22	5.23	0.05	14	5.15	0.0
CoI	2.95	0.20	1	2.87	0.12	10	2.88	–
CoII	2.61	0.09	9	–	–	–	2.61	–
NiI	3.92	0.12	3	3.94	0.16	18	3.94	–
NiII	3.94	0.04	5	–	–	–	3.94	–
ZnI	–	–	–	2.32	0.02	2	2.32	0.18
GeI	1.40	0.20	1	–	–	–	1.40	–
AsI	<0.84	–	1	–	–	–	<0.84	–
RbI	–	–	–	<2.42	–	5	<2.42	–
SrII	–	–	–	1.06	0.08	2	1.06	–
YII	0.58	0.20	1	0.46	0.13	9	0.48	–
ZrII	1.09	0.09	5	1.15	0.07	10	1.13	–
NbII	<0.93	–	1	–	–	–	<0.93	–
MoII	0.75	0.20	1	–	–	–	0.75	–
RuII	<1.54	–	1	–	–	–	<1.54	–
RhI	–	–	–	<1.52	–	5	<1.52	–
PdI	–	–	–	<1.34	–	5	<1.34	–
AgI	–	–	–	<1.38	–	5	<1.38	–
CdI	0.63	0.20	1	–	–	–	0.63	–
InII	<0.83	–	1	–	–	–	<0.83	–
SnI	<2.94	–	1	–	–	–	<2.94	–
TeI	<1.83	–	1	–	–	–	<1.83	–
BaII	–	–	–	0.48	0.06	5	0.48	–
LaII	–	–	–	–0.16	0.06	5	–0.16	–
CeII	–	–	–	0.24	0.03	2	0.24	–
PrII	–	–	–	–0.40	0.20	1	–0.40	–
NdII	–	–	–	0.17	0.12	6	0.17	–
SmII	–	–	–	0.18	0.2	1	0.18	–
EuII	–	–	–	–0.46	0.04	5	–0.46	–
GdII	0.40	0.20	1	0.38	0.04	2	0.38	–
TbII	–	–	–	<–0.06	–	6	<–0.06	–
DyII	–	–	–	0.26	0.09	5	0.26	–
HoII	–	–	–	–0.36	0.11	2	–0.36	–
ErII	–	–	–	0.12	0.19	2	0.12	–
TmII	–	–	–	–0.67	0.20	1	–0.67	–
YbII	–	–	–	–0.27	0.20	1	–0.27	–
LuII	–0.70	0.20	1	–	–	–	–0.70	–
HfII	–	–	–	<0.67	–	5	<0.67	–
OsII	0.49	0.20	1	–	–	–	0.49	–
IrI	<1.01	–	1	–	–	–	<1.01	–
PtI	0.60	0.13	2	–	–	–	0.60	–
AuI	–0.06	0.07	2	–	–	–	–0.06	–
ThII	–	–	–	<–0.38	–	6	<–0.38	–
UII	–	–	–	<0.43	–	5	<0.43	–
C-H	–	–	–	6.70	0.20	1	6.70	–
C-N	–	–	–	<7.73	–	5	<7.73	–

**Table 1.** Mean abundances ( $\log \epsilon(X)$ ), statistical uncertainty ( $\sigma_{stat}$ ), and the number of lines used (N) for each species in the UV and optical (op) domains. Also listed are the NLTE corrections for the mean abundances of each species, UV and optical lines considered together.

absorption feature has a potential contribution from both the  ${}^6\text{Li}$  and  ${}^7\text{Li}$  isotopes. We used an isotopic ratio of  ${}^6\text{Li}/{}^7\text{Li}=0.00$ , since any reasonable isotopic contribution from  ${}^6\text{Li}$  is undetectable at the resolution of our spectrum. For instance, increasing the isotopic ratio to 0.01, which is the upper limit suggested by Prantzos (2012) for metal-poor stars based on Galactic chemical evolution, did not change the line profile in any detectable manner. Moreover, it is recommended to implement 3D and NLTE models to reliably constrain the isotopic ratio from the spectral signature (Lind et al. 2013), which is beyond the scope of this work. However, we obtain a NLTE correction of  $-0.018$  using Breidablik<sup>8</sup> (Wang et al. 2021), which is an interpolation routine to estimate the NLTE correction of the Li abundance based on the EW of the line. For the final Li abundance, we adopted the NLTE-corrected abundance of  $\log \epsilon(\text{Li}) = 2.35$ .

## 6.2 C and N

We determined  $\log \epsilon(\text{C}) = 6.70$  using the CH *G*-band at 4313 Å. We also obtained an identical abundance using the C I  $\lambda 2964.85$  line. However, we don't find this line reliable in our spectrum since it is not very well resolved. Moreover, as pointed out by Roederer et al. (2022a), the accuracy of the line's  $\log gf$  value is graded a D ( $<50\%$ ;  $\pm 0.30$  dex) by NIST. Therefore, we adopted the C abundance from the CH *G*-band only. We further considered a correction to the C abundance due to possible CN processing as described in Placco et al. (2014), but find a correction of 0.0 dex<sup>9</sup> due to the relatively early evolutionary stage of the star.

For N, we used the  $\lambda 3876$  CN molecular band. However, the CN absorption features were very weak, so we determined a  $3\sigma$  upper limit, obtaining  $\log \epsilon(\text{N}) < 7.73$ .

## 6.3 Na, Al, and K

We determined  $\log \epsilon(\text{Na}) = 3.99$  using EW measurements of four Na I lines including the  $\lambda 5889/\lambda 5895$  and  $\lambda 8183/\lambda 8194$  doublets. We checked for telluric blending with the  $\lambda 8183/\lambda 8194$  doublet using the telluric spectrum provided with the Arcturus Atlas by Hinkle et al. (2000) and did not identify any strong blending. Moreover, the four Na I sodium lines render abundances in excellent agreement. We also estimated a NLTE correction of  $-0.10$  dex, based on NLTE correction grids provided by Lind et al. (2022). For the final Na abundance, we adopted the NLTE-corrected abundance of  $\log \epsilon(\text{Na}) = 4.09$ .

For Al, we could determine the abundance for two Al I lines in the optical and one Al II line in the UV using spectral synthesis. For the mean Al I abundance, we obtained  $\log \epsilon(\text{Al}) = 3.32$ . Specifically, we used spectral synthesis of Al I lines at 3944.00 Å and 3961.52 Å. On the other hand, we determined a much higher abundance of  $\log \epsilon(\text{Al}) = 4.21$  using the best-fit spectral synthesis model for the  $\lambda 2669.16$  Al II line, as shown in Figure 1 (Roederer & Lawler 2021). The reason for this discrepancy has been proposed to be NLTE effects on the abundances of low-excitation Al I lines, such as

Element	$\log \epsilon(\text{X})_{\odot}$	$\log \epsilon(\text{X})$	[X/Fe]	$\sigma_{\text{stat}}$	$\sigma_{\text{sys}}$	$\sigma_{\text{total}}$
Li	1.05	2.35	+3.65	0.20	0.05	0.21
O	8.69	6.98	+0.64	0.05	0.05	0.07
Na	6.24	3.89	-0.00	0.07	0.06	0.09
Mg	7.6	5.7	+0.45	0.20	0.08	0.22
Al	6.45	4.18	+0.08	0.20	0.06	0.21
Si	7.51	5.55	+0.39	0.08	0.05	0.09
S	7.12	<5.98	-	-	-	-
K	5.03	3.05	+0.37	0.20	0.05	0.21
Ca	6.34	4.62	+0.63	0.09	0.05	0.10
Sc	3.15	1.10	+0.30	0.05	0.05	0.07
Ti	4.95	3.12	+0.52	0.14	0.07	0.16
V	3.93	1.98	+0.40	0.07	0.06	0.09
Cr	5.64	3.43	+0.14	0.07	0.07	0.10
Mn	5.43	2.91	-0.17	0.08	0.05	0.09
Fe	7.5	5.15	+0.00	0.12	0.06	0.13
Co	4.99	2.61	-0.03	0.09	0.10	0.14
Ni	6.22	3.94	+0.07	0.04	0.09	0.1
Zn	4.56	2.50	+0.29	0.02	0.04	0.04
Ge	3.65	1.40	+0.10	0.20	0.17	0.26
As	2.3	<0.84	-	-	-	-
Rb	2.52	<2.42	-	-	-	-
Sr	2.87	1.06	+0.54	0.08	0.18	0.20
Y	2.21	0.48	+0.62	0.13	0.06	0.14
Zr	2.58	1.13	+0.90	0.08	0.06	0.10
Nb	1.46	<0.93	-	-	-	-
Mo	1.88	0.75	+1.22	0.2	0.05	0.21
Ru	1.75	<1.54	-	-	-	-
Rh	0.91	<1.52	-	-	-	-
Pd	1.57	<1.34	-	-	-	-
Ag	0.94	<1.38	-	-	-	-
Cd	1.71	0.63	+1.27	0.20	0.13	0.24
In	0.8	<0.83	-	-	-	-
Sn	0.8	<0.83	-	-	-	-
Te	2.18	<1.83	-	-	-	-
Ba	2.18	0.48	+0.65	0.06	0.05	0.08
La	1.1	-0.16	+1.09	0.06	0.06	0.09
Ce	1.58	0.24	+1.01	0.03	0.05	0.05
Pr	0.72	-0.40	+1.23	0.20	0.20	0.28
Nd	1.42	0.17	+1.10	0.12	0.11	0.16
Sm	0.96	0.18	+1.57	0.20	0.07	0.21
Eu	0.52	-0.46	+1.37	0.04	0.05	0.07
Gd	1.07	0.38	+1.66	0.03	0.15	0.15
Tb	0.30	<-0.06	-	-	-	-
Dy	1.10	0.26	+1.51	0.09	0.09	0.13
Ho	0.48	-0.36	+1.51	0.11	0.07	0.13
Er	0.92	0.12	+1.55	0.19	0.10	0.21
Tm	0.10	-0.67	+1.58	0.20	0.06	0.21
Yb	0.84	-0.27	+1.24	0.20	0.05	0.21
Lu	0.10	-0.7	+1.55	0.20	0.17	0.26
Hf	0.85	<0.67	-	-	-	-
Os	1.40	0.49	+1.44	0.20	0.29	0.35
Ir	1.38	<1.01	-	-	-	-
Pt	1.62	0.6	+1.33	0.13	0.13	0.19
Au	0.92	-0.06	+1.37	0.07	0.12	0.14
Th	0.02	<-0.38	-	-	-	-
U	-0.54	<0.43	-	-	-	-
C-H	8.43	6.7	+0.62	0.20	0.12	0.23
C-N	7.83	<7.73	-	-	-	-

**Table 2.** Adopted and recommended abundances for 2MASS J00512646-1053170, along with statistical ( $\sigma_{\text{stat}}$ ), systematic ( $\sigma_{\text{sys}}$ ), and total uncertainty ( $\sigma_{\text{tot}}$ ). The Solar abundances of the elements ( $\log \epsilon(\text{X})_{\odot}$ ) are taken from Asplund et al. (2009).

<sup>8</sup> <https://github.com/ellawang44/Breidablik>

<sup>9</sup> Using the online tool available at <http://vplacco.pythonanywhere.com/>

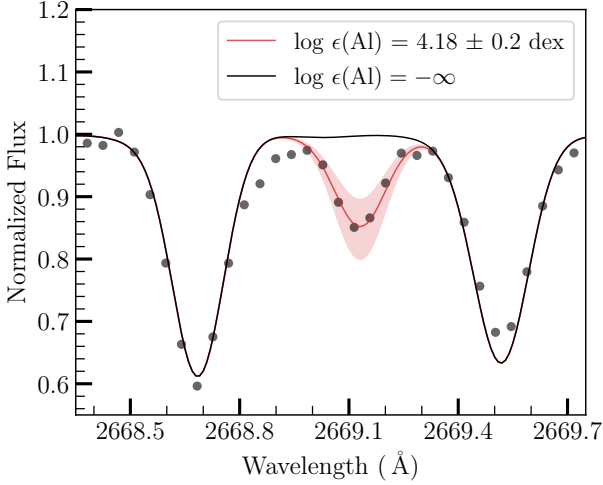


**Figure 1.** The best-fit spectral synthesis model for the Al II line at 2669.16 Å is shown with a red-solid line, with the observed data shown in black points. The red-shaded region depicts abundance variation within  $\pm 0.2$  dex of the best-fit abundance. The black-solid line traces the synthetic model with no contribution from Al.

those used here, on the order of  $\sim +0.4$  dex for metal-poor main-sequence turn-off stars (Nordlander & Lind 2017; Roederer & Lawler 2021). On the other hand, the ground state  $\lambda 2669.16$  Al II line is considered to be forming in LTE, providing a more faithful Al abundance determination (Mashonkina et al. 2016; Roederer & Lawler 2021). Indeed, we estimated a NLTE correction of  $+0.47$  dex for Al I based on the NLTE correction grids provided by Mashonkina et al. (2016). However, in spite of this large NLTE correction, the NLTE corrected Al I is still much lower than the Al II abundance. Therefore, for the final Al abundance, we adopted the Al II abundance of  $\log \epsilon(\text{Al}) = 4.21$ .

We determined  $\log \epsilon(\text{K}) = 3.33$  using EW measurement of the K I line at 7698.96 Å. While we also detected absorption at the  $\lambda 7664.90$  K I line, it appears to be contaminated with telluric blends. We estimated a NLTE correction of  $-0.28$  dex for the K I abundance, based on the NLTE grids provided by Takeda et al. (2002) for the  $\lambda 7698$  K I line. For the final K abundance, we adopted the NLTE-corrected abundance of K I, which was  $\log \epsilon(\text{K}) = 3.05$ .

#### 6.4 $\alpha$ -Elements: O, Mg, Si, S, and Ca

For O, we determined  $\log \epsilon(\text{O}) = 7.08$  using spectral synthesis of the O I triplet near 7770 Å. We also estimated a NLTE correction of  $-0.10$  dex, based on the 1D NLTE correction grids provided by Amarsi et al. (2016a) for the middle O I triplet line in a turn-off star. For the final O abundance, we adopted the NLTE-corrected abundance of  $\log \epsilon(\text{O}) = 6.08$ .

For Mg, we determined the abundances for 7 Mg I lines in the optical, 2 Mg I lines in the UV, and one Mg II line in the UV, all using spectral synthesis. We obtained  $\log \epsilon(\text{Mg}) = 5.73$  and  $\log \epsilon(\text{Mg}) = 5.72$ , with the optical and UV Mg I lines, respectively. Furthermore, we corrected the mean Mg I abundance from these 9 lines for NLTE effects using the Mg I grid provided by Lind et al. (2022). We obtained a correction of  $+0.10$  dex, bringing the NLTE Mg I abundance to

$\log \epsilon(\text{Mg}) = 5.83$ . For the Mg II line at  $\lambda 2828$ , we obtained  $\log \epsilon(\text{Mg}) = 5.70$ , in agreement with the LTE as well as the NLTE abundance Mg I abundance. For the final Mg abundance, we adopted the Mg II abundance.

For Si, we determined abundances for Si I and Si II lines in the UV and optical spectra using spectral synthesis. While we detected several Si I lines in the UV spectrum, most were too strong for reliable abundance determination. Aside from the strong lines, two Si I lines at 2438.77 Å and 2443.36 Å yielded Si abundance  $\sim 0.4$  dex higher than that determined from other Si I and Si II lines. It is unclear why this is the case, since the excitation potential of these lines, 0.00 and 0.01 eV, respectively, are only slightly lower than that of the other Si I lines investigated, which have excitation potentials in the range of 0.78 - 1.91 eV. Therefore, we excluded these lines for the purpose of abundance determination, and suggest caution when using these lines. As a result, we used one line from the UV and one from the optical to obtain a mean Si I abundance of  $\log \epsilon(\text{Si}) = 5.56$ . We also estimated a NLTE correction for the optical Si I line at 3905.53 Å using the MPIA-based NLTE correction tool<sup>10</sup>, which yielded a correction of  $+0.003$  dex based on the NLTE model grids provided by Bergemann et al. (2013). We assume a similar NLTE correction for the UV Si I line and consider  $+0.003$  dex to be the NLTE correction for the mean Si I LTE abundance.

For the mean Si II abundance, we used two Si II lines in the UV and one Si II line in the optical, which yielded  $\log \epsilon(\text{Si}) = 5.55$ . We find that the Si II abundance is in excellent agreement with the Si I LTE abundance. On the other hand, Roederer et al. (2016) and Roederer et al. (2022a) found that the low-excitation Si I lines yielded lower Si abundances than the high-excitation Si I lines and the Si II lines. We suspect that the better agreement observed for J0051-1053 might be in part due to the higher  $\log g$  of the star, resulting in lower NLTE effects for the low-excitation Si I lines. For the final Si abundance, we adopted the Si II abundance.

We inspected three S I lines in the  $\lambda 6700$  region (Roederer et al. 2022a), but could not determine a reliable S abundance or upper limit.

We determined the Ca abundance using EW measurements of 24 Ca I lines in the optical and obtained  $\log \epsilon(\text{Ca}) = 4.48$ . We also included a NLTE correction of  $+0.26$  dex, as computed by Mashonkina et al. (2017) for HD 84937, which has similar stellar parameters as J0051-1053. For the final Ca abundance, we used the NLTE-corrected value of  $\log \epsilon(\text{Ca}) = 4.74$ .

#### 6.5 Fe-group Elements: Sc, Ti, V, Cr, Mn, Fe, Co, Ni, and Zn

We determined the Sc abundance using spectral synthesis of 12 Sc II lines in the optical and one Sc II line in the UV, which yielded  $\log \epsilon(\text{Sc}) = 1.10$  and  $\log \epsilon(\text{Sc}) = 1.13$ , respectively. We used all 13 lines to determine the mean Sc abundance of J0051-1053.

We determined the Ti abundance using EW measurements of 34 Ti II lines in the optical, which yielded  $\log \epsilon(\text{Ti}) = 3.12$ , and spectral synthesis of 5 Ti II lines in the UV, which yielded  $\log \epsilon(\text{Ti}) = 3.10$ . We also determined a similar abundance of

<sup>10</sup> [https://nlte.mpia.de/gui-siuAC\\_secE.php](https://nlte.mpia.de/gui-siuAC_secE.php)

$\log \epsilon(\text{Ti}) = 3.20$  from EW measurements of 12 Ti I lines in the optical. Based on the NLTE analysis of Ti lines in HD 84937 by [Sitnova et al. \(2020\)](#), we estimated a NLTE correction of +0.14 and +0.04 dex for Ti I and Ti II in J0051-1053, respectively. Given the negligible NLTE effects on Ti II, for the final Ti abundance we adopted the LTE Ti II abundance of  $\log \epsilon(\text{Ti}) = 3.12$ .

We determined the V abundance using spectral synthesis of 7 V II lines in the optical and 6 V II lines in UV, which yielded  $\log \epsilon(\text{V}) = 1.97$  and  $\log \epsilon(\text{V}) = 1.99$ , respectively. We were also able to determine  $\log \epsilon(\text{V}) = 2.05$  using the  $\lambda 4111$  V I line, which agrees very well with the V II abundance. We note that NLTE grids for V I and V II are presently not available in the literature. For the final V abundance, we adopted the mean abundance from the 13 V II lines.

For Cr, we determined abundances for Cr I and Cr II lines in the UV and optical spectra with spectral synthesis. We determined  $\log \epsilon(\text{Cr}) = 3.31$  with Cr I lines and  $\log \epsilon(\text{Cr}) = 3.42$  using the Cr II line, which agree. We note that the mean Cr II abundance from 11 lines in the UV is +0.15 dex higher than the mean Cr II abundance from 3 lines in the optical. However, since the discrepancy is on the order of uncertainties on the Cr abundance ( $\sim 0.10$  dex), we don't suspect anything unusual at play. We also considered a NLTE correction of +0.25 dex and +0.04 dex for Cr I and Cr II, respectively, based on the NLTE analysis of HD 84937 by [Bergemann & Cescutti \(2010\)](#). Since the NLTE correction for Cr II is negligible, for the final Cr abundance we adopted the mean LTE Cr II abundance from 11 Cr II lines in UV and 3 Cr II lines in optical, which was  $\log \epsilon(\text{Cr}) = 3.43$ .

For Mn, we determined abundances for Mn I and Mn II lines in the UV and optical spectra. We avoided the triplet Mn I resonance lines in the  $\lambda 4030$  region since these yielded abundances  $\sim 0.20$  dex lower than the higher-excitation lines. The systematically lower abundances obtained with the Mn triplet, relative to other higher-excitation Mn I lines, has been well-documented (e.g., [Cayrel et al. 2004](#); [Roederer et al. 2010a](#); [Snedden et al. 2023](#)). We find that the mean Mn II abundance is slightly higher than the mean Mn I abundance, but the discrepancy is within uncertainties. We estimated a NLTE correction of +0.28 and  $-0.03$  dex for the Mn I and Mn II abundances, respectively, based on the NLTE grids provided by [Bergemann et al. \(2019\)](#). For the final Mn abundance, we adopted the mean LTE Mn II abundance of  $\log \epsilon(\text{Mn}) = 2.91$  from 2 UV lines and 4 optical lines.

For Fe, we determined abundance for Fe I and Fe II lines in the UV using spectral synthesis and for Fe I and Fe II lines in the optical using EW measurements. For Fe I, we determined abundances for 21 lines in the UV and 156 lines in the optical, and obtained a mean Fe I abundance of  $\log \epsilon(\text{Fe}) = 5.19$ . For Fe II, we determined abundances for 22 lines in the UV and 14 lines in the optical, and obtained a mean Fe II abundance of  $\log \epsilon(\text{Fe}) = 5.15$ , which agrees very well with the mean Fe I abundance. We note that the mean Fe II abundance with the UV lines is +0.13 higher than the mean Fe II abundance obtained with the optical lines (see Table 1). However, since the standard deviation in the abundances of the UV lines is 0.12, on the same order as the difference in the mean UV and optical abundances, we don't consider this discrepancy to be of concern. We also considered a NLTE correction of +0.17 dex for Fe I and 0.0 dex for Fe II, based on the NLTE analysis of HD 84937 by [Amarsi et al. \(2016b\)](#). For the final

Fe abundance, we adopted the LTE Fe II abundance from the UV and optical lines.

We determined abundances for Co I lines in the UV and optical spectra as well as for Co II lines, which are available only in the UV spectrum. We obtained a significantly higher mean Co I abundance of  $\log \epsilon(\text{Co}) = 2.88$  than the mean Co II abundance of  $\log \epsilon(\text{Co}) = 2.61$ . A similar discrepancy was observed by [Cowan et al. \(2020\)](#) for three other turn-off stars with HST/STIS UV spectra. On the other hand, [Roederer et al. \(2022a\)](#) did not observe such a discrepancy in the giant HD 222925. We further obtained a NLTE correction on the order of +0.89 dex for the Co I lines used here using the [Bergemann et al. \(2010\)](#) grids<sup>11</sup>, which exacerbates the discrepancy. We note that given the high NLTE corrections obtained and the absence of an explicit analysis of a turn-off metal-poor star in the study, it is unclear whether the grid reliably extends to temperatures as high as 6400 K and metallicity as low as  $-2.28$ . We are expecting new NLTE studies for Co in the near future. Nevertheless, we adopted the mean abundance from 9 Co II lines in the UV.

We determined abundances for Ni I lines in the UV with spectral synthesis and for Ni I lines in the optical with EW measurements. We also determined abundances for Ni II lines in the UV using spectral synthesis. The mean Ni I abundance of  $\log \epsilon(\text{Ni}) = 3.94$  from 18 lines in the optical and 3 lines in the UV is the same as the Ni II abundance of from 18 lines in the UV, indicating small NLTE effects for Ni I. For the final Ni abundance, we adopted the mean Ni II abundance of  $\log \epsilon(\text{Ni}) = 3.94$ .

We looked for a Cu I signature at the  $\lambda 5105$  line, however, we could not determine a reliable detection.

Lastly, for this group of elements, we determined  $\log \epsilon(\text{Zn}) = 2.32$  with spectral synthesis of two Zn I lines in the optical. We estimated a +0.18 dex NLTE correction on the Zn abundance using the NLTE grids provided by [Sitnova et al. \(2022\)](#) for the  $\lambda 4810$  Zn I line. For the final Zn abundance, we adopted the NLTE-corrected abundance of Zn I, which results in  $\log \epsilon(\text{Zn}) = 2.50$ .

## 6.6 Elements at the First *R*-Process Peak

Of the elements near the first *r*-process peak, including Ga, Ge, As, and Se, the transitions of Ga and Se were out of the spectral range. For Ge, we determined  $\log \epsilon(\text{Ge}) = 1.40$  using the  $\lambda 3039$  Ge I line. We show the spectral synthesis fit to the region in Figure 2. The spectral synthesis fit is not exact, possibly due to noise in the spectrum. Therefore, we assigned an additional 0.10 dex uncertainty for the Ge abundance. For As, we could only determine a  $3\sigma$  upper limit of  $\log \epsilon(\text{As}) < 0.84$  using the  $\lambda 2288$  As I line.

## 6.7 Elements Between the First and Second *R*-Process Peaks

These elements include Rb ( $Z = 37$ ), Sr ( $Z = 38$ ), Y ( $Z = 39$ ), and Zr ( $Z = 40$ ). For Rb, we could not detect significant absorption, and thereby determined a  $3\sigma$  upper limit using the  $\lambda 7947$  Rb I line. For Sr, we determined  $\log \epsilon(\text{Sr}) = 1.05$

<sup>11</sup> We used the MPIA NLTE tool online at [https://nlte.mpia.de/gui-siuAC\\_secE.php](https://nlte.mpia.de/gui-siuAC_secE.php) for interpolating the grids



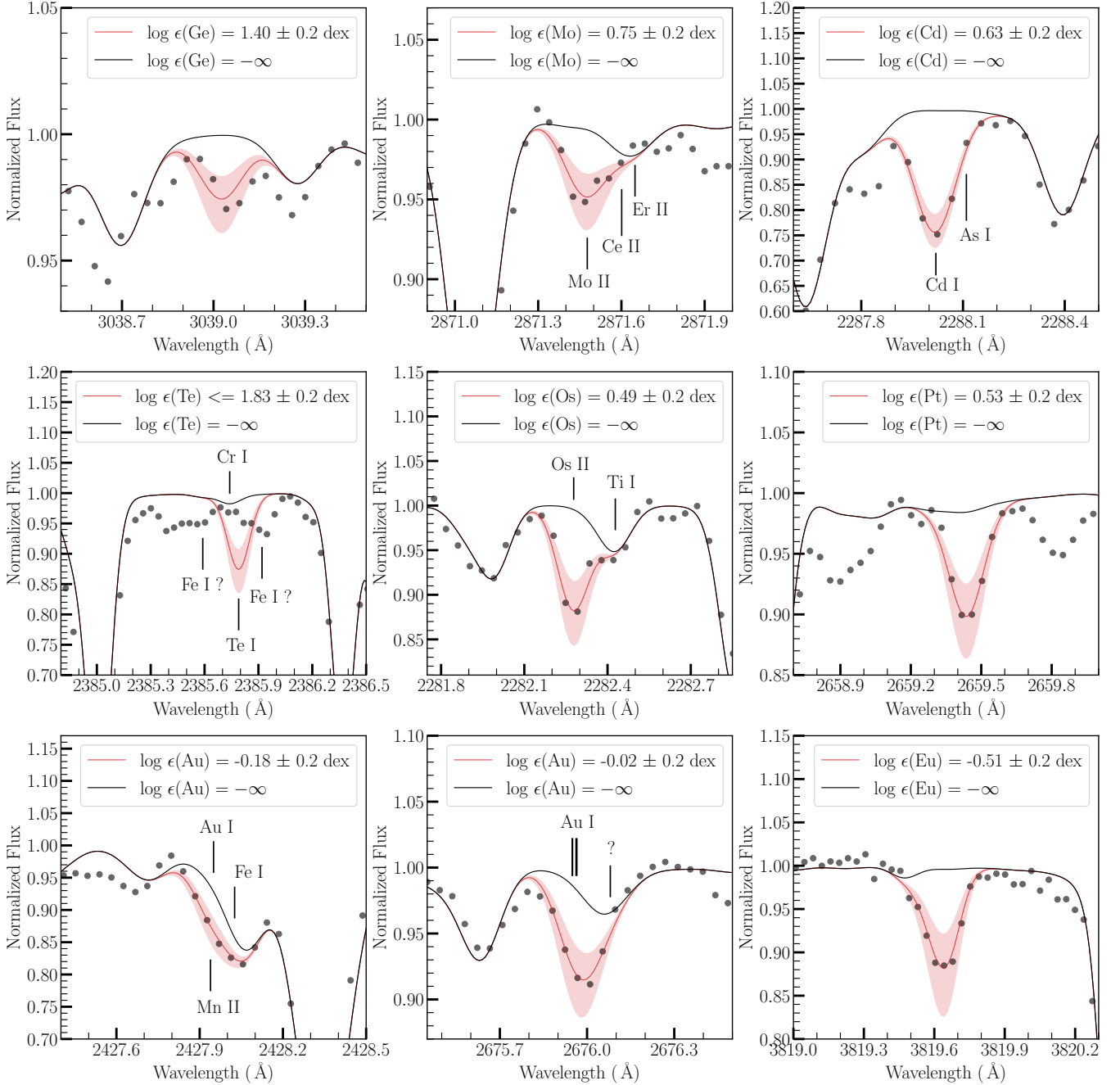


**Figure 2.** Spectral synthesis fits to absorption lines of various  $r$ -process elements. The red-solid line traces the best-fit synthetic model to the observed data in black points. The red-shaded shaded region depicts abundance variation within  $\pm 0.2$  dex of the best-fit abundance. The black-solid line traces the synthetic model with no contribution from the relevant element. Important neighboring absorption lines are also labeled.

using two Sr II transitions in the optical. For Y, we obtained  $\log \epsilon(\text{Y}) = 0.58$  using one Y II line in the UV and  $\log \epsilon(\text{Y}) = 0.46$  using 9 Y II lines in the optical. Since the mean UV and the mean optical Y II abundances agree within their statistical uncertainties, we adopted the mean from all 10 lines as the Y abundance. Similarly, we determined the Zr abundance for 5 Zr II lines in the UV ( $\log \epsilon(\text{Zr}) = 1.09$ ) and 10 Zr II lines in the optical ( $\log \epsilon(\text{Zr}) = 1.15$ ), and we adopted the mean of all 15 lines as the Zr abundance.

For Nb, we detected only a faint absorption signature for the Nb II at 2927.81 Å in the UV. Moreover, the blends were neither resolved nor constrained well by our synthetic spectrum. As a result, we could only determine a  $3\sigma$  upper limit. For Mo, we determined  $\log \epsilon(\text{Mo}) = 0.71$  using the Mo II line at 2871.51 Å in the UV. The other Mo lines were too weak for abundance determination, including the Mo I transitions in the optical. Figure 2 shows the spectral synthesis fit to the  $\lambda 2971$  line.

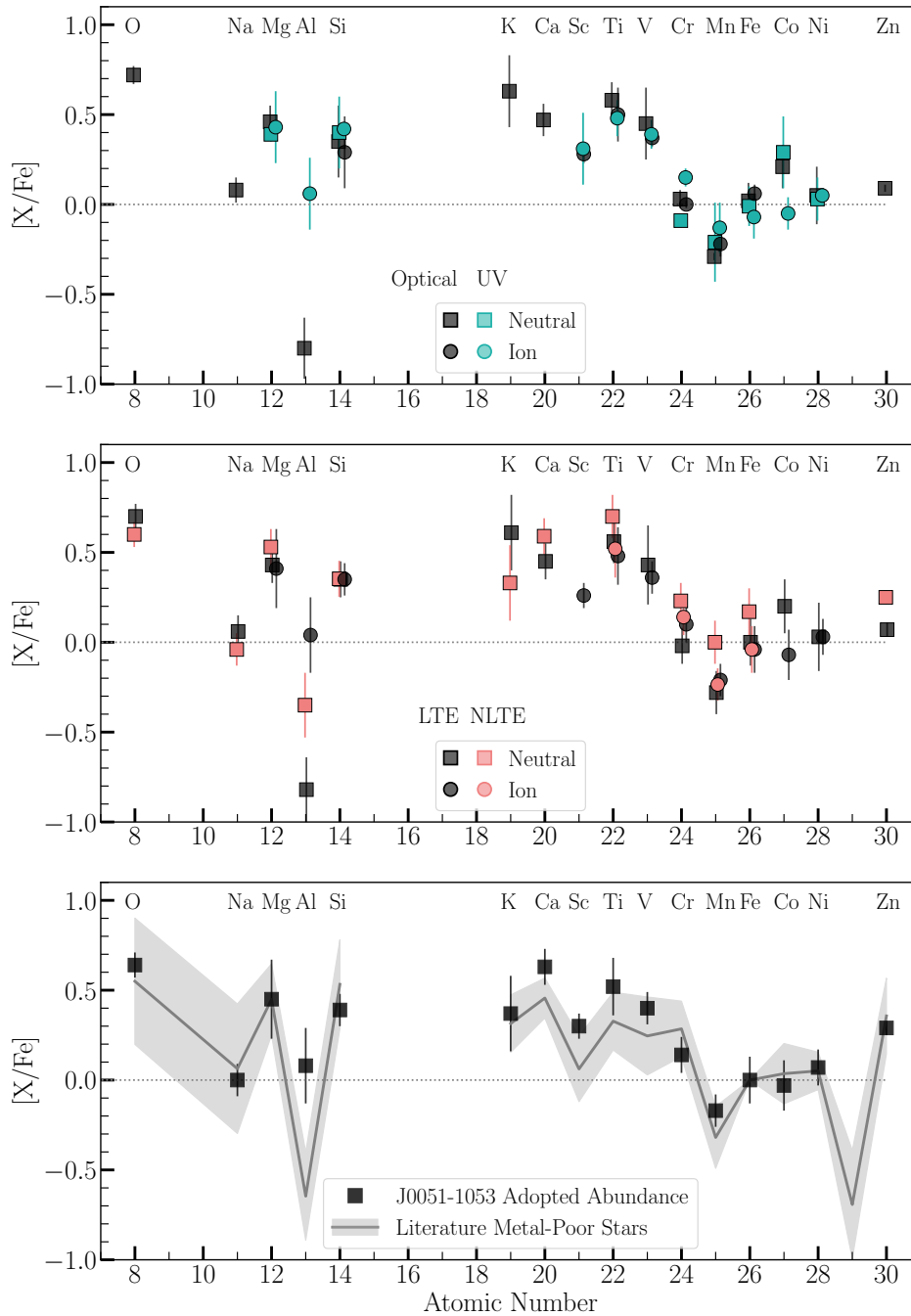


**Figure 3.** Top Panel: Mean  $[X/Fe]$  abundances of light-element species from the UV (green points) and optical spectra (black points). Middle Panel: Mean LTE (black points) and NLTE-corrected (red points) abundances of light-element species. Bottom Panel: The adopted abundances of the light elements for J0051-1053 are shown with black-square points. The black-solid line traces the mean  $[X/Fe]$  abundances of these elements for the metal-poor stars analyzed in [Roederer et al. \(2014a\)](#). The grey-shaded region traces the corresponding standard deviation in the  $[X/Fe]$  abundances for the [Roederer et al. \(2014a\)](#) sample.

We did not detect any clean strong absorption line of Ru I or Ru II in the UV or in the optical. Therefore, we determined a  $3\sigma$  upper limit for the Ru abundance using the  $\lambda 2456$  Ru II line. Similarly for Rh, we investigated 6 Rh I lines in the optical, but did not detect a reliable signature for abundance determination. Therefore, we determined a  $3\sigma$  upper limit for Rh using the  $\lambda 3435$  line. The trend continued for Pd and Ag, for which we could also only determine  $3\sigma$  upper lim-

its using the  $\lambda 3405$  Pd I and  $\lambda 3382$  Ag I lines. In particular, for the Pd I and Ag I lines, the neighboring blends were not well-constrained or resolved.

For Cd, we determined  $\log \epsilon(\text{Cd}) = 0.63$  with the  $\lambda 2288$  Cd I line. While this line is blended with the  $\lambda 2288$  As I line, the signature of As is negligible in the spectrum of J0051-1053; the Cd-As absorption feature could be fit best by just

the Cd abundance. Figure 2 shows the spectral synthesis fit to the Cd line.

For In, we determined a  $3\sigma$  upper limit using the In II line at 2306.06 Å. Unfortunately, it is blended with a Fe II line at 2306.17 Å with an uncertain  $\log gf$ -value (Roederer et al. 2022a) and features a very weak absorption signature in the spectrum of J0051-1053. For Sn, we detected a possible signature at the  $\lambda 2287$  Sn I line, however, it was too noisy to yield a reliable abundance or upper limit.

### 6.8 Second *R*-Process Peak: Te

The Te I line at 2385.79 Å is not resolved in the spectrum of J0051-1053 and features a very weak absorption signature (see Figure 2). Furthermore, the neighboring lines at 2385.59 Å and 2385.92 Å, which are possibly Fe I lines or at least have contribution from them, are not fit well and are blended with the Te I line. There is additional contribution to the Te I feature from a Cr I line at 2385.74 Å. Given the difficulty to reliably constrain the contribution from Te in this spectral region, we determined a  $3\sigma$  upper limit of  $\log \epsilon(\text{Te}) < 1.83$  for the Te abundance. We show the upper limit model for Te in Figure 2.

### 6.9 Ba, Lanthanides, and Hf

For elements in this group, we determined abundances for all, except for Sm, Tb, and Hf, for which we could only determine upper limits.

For Ba, we used 5 Ba II transition lines in the optical, which were strong and provided a precise mean abundance. For La, the line strengths were relatively weaker, but 5 La II transitions were strong enough to obtain reliable abundance determinations. For Ce, we used two Ce II lines to determine the abundance. In general, the other lines were either too weak and/or unresolved, and the contribution from Ce was difficult to constrain. For Pr, we determined the abundance using the Pr II line at 4225.32 Å.

For Nd, we determined the abundance using 6 Nd II lines in the optical. For Sm, unfortunately, the strongest lines were still weak based on our detection threshold (see Section 7). Therefore, we obtained only a  $3\sigma$  upper limit on the Sm abundance using the Sm II line at 4329.02 Å. For Eu, we used 5 Eu II lines in the optical, all of which lend Eu abundance within  $\pm 0.10$  dex of each other.

For Gd abundance, we used two Gd II lines in the optical and one Gd II line in the UV. All three lines lend Gd abundance within  $\pm 0.05$  dex of each other. The  $\lambda 3032$  Gd II line in the UV is blended with a Sn I line at 3032.79 Å and a Cr I line at 3029.16 Å. The Cr I line is the dominant source of absorption in this Sn-Gd-Cr feature, but mainly affects the red wing, while the Gd line affects the blue wing. The Sn line is also situated blue and has a direct impact on the Gd abundance. Since the Sn I lines are extremely weak, if not undetectable in the spectrum of J0051-1053, we neglect the Sn contribution to this feature (see Section 6.7). Furthermore, we added an additional  $\pm 0.15$  dex component to the systematic uncertainty of this line to compensate for the uncertain contribution of Sn.

For Tb, we detected a weak absorption signature at the 3874.17 Å Tb II line, but its signature is below our detection

threshold (Section 7). As a result, we determined a  $3\sigma$  upper limit for the abundance. For Dy, Ho, Er, Tm, and Yb we used 5 Dy II, 2 Ho II, 2 Er II, one Tm II, and one Yb II absorption lines, respectively, in the optical spectrum.

For Lu, we used the Lu II line at 2615.14 Å in the UV spectrum, which displayed a strong signature. The HFS pattern for the line was adopted from Den Hartog et al. (2020). The Lu II lines in the optical did not display any detectable absorption. While the  $\lambda 2615$  UV Lu II is strong, Roederer et al. (2022b) identified that this line is blended with an unknown transition. They showed that this blend primarily affected stars with low levels of *r*-process enhancement, and would result in an unusually high  $\log \epsilon(\text{Lu}/\text{Eu})$  ratio of  $\gtrsim 0.5$ . Since J0051-1053 is highly *r*-process enhanced, with  $[\text{Eu}/\text{Fe}] = +1.37$ , we suspect that the unidentified blend, if present, will have a marginal impact on the Lu abundance. Moreover, upon fitting the Lu feature without accounting for the blend, we obtained  $\log \epsilon(\text{Lu}) = -0.70$  and  $\log \epsilon(\text{Lu}/\text{Eu}) = -0.35$ . Roederer et al. (2022a) determined a similar ratio of  $\log \epsilon(\text{Lu}/\text{Eu}) = -0.40$  for HD 222925 using other Lu II lines. Nevertheless, for caution, we added an additional  $\pm 0.10$  dex of systematic uncertainty on the derived Lu abundance.

We checked for several Hf II lines in the UV and optical spectra, but could not determine a reliable absorption signature. Therefore, we determined an upper limit of  $\log \epsilon(\text{Hf}) < +0.67$ .

### 6.10 Third *R*-Process Peak: Os, Pt, and Au

We determined the Os abundance using the Os II line at 2282.28 Å in the UV spectrum. The line is situated between an Fe I line at 2281.99 Å and a Ti I line at 2282.43 Å. We adjusted the oscillator strength of these neighboring lines to fit their lines, but we note that these changes did not impact the fit to the Os line and its derived abundance. We used the  $\log gf$  value for the Os line from Quinet et al. (2006). However, Ivarsson et al. (2004) also provided the  $\log gf$  value for this line, reporting a value lower by  $\sim -0.10$  dex. Therefore, we added a  $\pm 0.10$  dex systematic uncertainty on the Os abundance from the uncertainty in its  $\log gf$  value.

For Ir, we determined a  $3\sigma$  upper limit using the Ir I at 2639.71 Å in the UV, since the signature of the line was weak and unresolved.

We determined the Pt abundance using two Pt I lines in the UV at 2659.43 Å and 2997.96 Å. We suspect that there may be an unidentified blend to the  $\lambda 2997.96$  line (see also Figure 4 of Den Hartog et al. 2005), especially since the abundance from this line is higher by 0.15 dex than the abundance from the  $\lambda 2659.43$  line. Therefore, we included an additional  $\pm 0.10$  dex systematic uncertainty on this line abundance. The atomic parameters for both the lines, including HFS and IS, were taken from Den Hartog et al. (2005). While we detected absorption signatures at some other Pt I lines listed in Den Hartog et al. (2005), the lines were either not well-resolved or weak.

For the Au abundance, we used the Au I resonance lines at 2427.95 Å and 2675.95 Å. The  $\lambda 2427.95$  line is blended with an Fe II line at 2428.08 Å, which contributes to the red side of the Au-Fe absorption signature, but constrains the data well. The  $\log gf$  value for this Au I line was taken from Hannaford et al. (1981), with NIST ASD quoting a grade B+

(7%,  $\pm 0.05$  dex uncertainty). For the  $\lambda 2676$  Au I line, we used the HFS line component provided by [Roederer et al. \(2022a\)](#). The log  $gf$  value of the line was also taken from [Hannaford et al. \(1981\)](#), but for this line, NIST ASD quotes a higher accuracy of A+ (2%,  $\pm 0.02$  dex uncertainty). In our spectrum, this line is primarily blended with an unidentified line. Since the resolution of our spectrum is not high enough to resolve the blend from the Au I line, we used the atomic parameters of this unidentified blend as constrained by [Roederer et al. \(2022a\)](#) for HD 222925. This Au I line is also blended with a Nb II line at  $2675.94 \text{ \AA}$ , for which we estimated a negligible contribution, since the Nb lines in J0051-1053 appear almost undetectable. As a final note, we blue-shifted the wavelength of the  $\lambda 2676$  Au line component by  $0.04 \text{ \AA}$  from the original center-of-gravity wavelength reported in NIST. The need for a similar wavelength shift was discussed in [Roederer et al. \(2022a\)](#) for HD 222925, but the cause is unclear.

### 6.11 Actinides

We did not detect any signature of Th or U at any of the Th II and U II lines, including the recently analyzed U II lines at  $4050.04 \text{ \AA}$  and  $4090.23 \text{ \AA}$  ([Shah et al. 2023](#)). Therefore, we obtained  $3\sigma$  upper limits for the Th abundance. We do not report the upper limit for U since the spectral regions of the lines were noisy, preventing a constraining upper limit determination.

## 7 DETECTION THRESHOLD AND UPPER LIMITS

Due to the high temperature of the star, several absorption lines of the  $r$ -process elements are weak and exhibit absorption depths comparable to the noise level of the spectrum. In order to enable a reliable abundance determination from these weak lines, we employed a minimum EW ( $EW_{limit}$ ) as the detection threshold. We obtained  $EW_{limit}$  using the Cayrel formula for uncertainty on the EW of a weak line ( $\sigma_{EW}$ ), as given by equation 2 ([Cayrel 1988](#); [Cayrel et al. 2004](#)). Here  $\delta x$  is the width of the pixel in  $\text{\AA}$ , which is  $\sim 0.04 \text{ \AA}$  for both the UV and optical spectrum. We then obtained  $EW_{limit}$  as  $2\sigma_{EW}$ , as shown in equation 3.

$$\sigma_{EW} = \frac{1.5}{S/N} \sqrt{FWHM * \delta x} \quad (2)$$

$$EW_{limit} = 2\sigma_{EW} \quad (3)$$

With this method, the  $EW_{limit}$  is  $1.6 \text{ m\AA}$  for the UV spectrum and  $3.8 \text{ m\AA}$  for the optical spectrum. Therefore, we only use lines that have EWs, as obtained from the best-fit spectral synthesis model, larger than the  $EW_{limit}$  of the respective spectrum. In general, most of the weak lines used for abundance determination have EWs larger than  $3\sigma_{EW}$ . One notable exception is the  $\lambda 3039$  Ge I line, which has an EW measurement of  $2.1\sigma_{EW}$ . We further discuss the abundance determination with this line in Section 9.2.1. In addition to this detection threshold, we take into account unknown blends and the overall fit to the spectral region when using a line for abundance determination.

For elements that did not have any lines with signatures beyond the detection threshold, we determined a  $3\sigma$  upper

limit on the element abundance with a suitable line of the element. The most suitable line for upper-limit determination was chosen based on the strength of the line, the SNR in the spectral region, and the constraint on the neighboring lines. Specifically, the  $3\sigma$  upper limit was obtained such that the least  $\chi^2$  value of the upper-limit spectral-synthesis model was higher than the least  $\chi^2$  value of the best-fit spectral-synthesis model by  $3\sigma$ , where  $\sigma$  is the spectral noise of the data.

## 8 UNCERTAINTY ANALYSIS

To determine the total uncertainty ( $\sigma_{tot}$ ) on the abundance of an element, we took into account statistical uncertainties ( $\sigma_{stat}$ ), which represented uncertainties in the determination of the atomic parameters of the lines, and systematic uncertainties ( $\sigma_{sys}$ ), which represented uncertainties in the stellar parameters and line fits. These are listed in Table 2. We added the  $\sigma_{stat}$  and  $\sigma_{sys}$  uncertainties in quadrature to obtain  $\sigma_{tot}$ .

For  $\sigma_{stat}$ , we used the standard deviation in the abundances from individual lines, in the cases 6 or more lines were used ( $N \geq 6$ ). In case,  $2 \leq N \leq 5$ , we obtained  $\sigma_{stat}$  by multiplying the range of the abundances with the  $k$ -factor from [Keeping \(1962\)](#), to compensate for the small samples and obtain more realistic uncertainty estimates (e.g., [Cain et al. 2018](#)). In the case  $N = 1$ , we assigned a fiducial uncertainty of  $\pm 0.20$  dex to  $\sigma_{stat}$ .

For  $\sigma_{sys}$ , we accounted for uncertainties from stellar parameters,  $T_{eff}$ , log  $g$ ,  $\xi$ , and [Fe/H] and additional uncertainties from spectral-synthesis fitting due to blends, uncertain atomic parameters, or uncertain continuum placement (see Section 6 for details). We first obtained  $\sigma_{sys}$  for each line and then took their average,  $\langle \sigma_{sys} \rangle$ , to represent the systematic uncertainty on the mean abundance of the element, which we list in Table 2. To obtain the uncertainties from the stellar parameters, we individually changed  $T_{eff}$ , log  $g$ ,  $\xi$ , and [Fe/H] by  $\pm 82 \text{ K}$ ,  $\pm 0.07 \text{ dex}$ ,  $\pm 0.2 \text{ km/s}$ , and  $\pm 0.2 \text{ dex}$ , respectively. We added the uncertainties from each of the stellar parameters as well as the uncertainty from the spectral models in quadrature to obtain  $\sigma_{sys}$  for each line.

For the final systematic uncertainty of a species, we used the average of the systematic of species' transitions. The statistical and systematic uncertainties for the adopted abundances are listed in Table 2.

## 9 DISCUSSION

### 9.1 Light Elements

Among the light elements with  $Z \leq 30$ , we obtained abundances for 16 elements, including 26 species. In the following sections, we discuss the abundances from the UV and optical lines (section 9.1.1), the observed NLTE effects and theoretical corrections (section 9.1.2), and the adopted abundances of J0051-1053 compared to that of other metal-poor stars from [Roederer et al. \(2014a\)](#) (section 9.1.3).

#### 9.1.1 UV and Optical Abundances

The UV spectral coverage enabled us to determine abundances of 4 unique species, which are generally not detectable

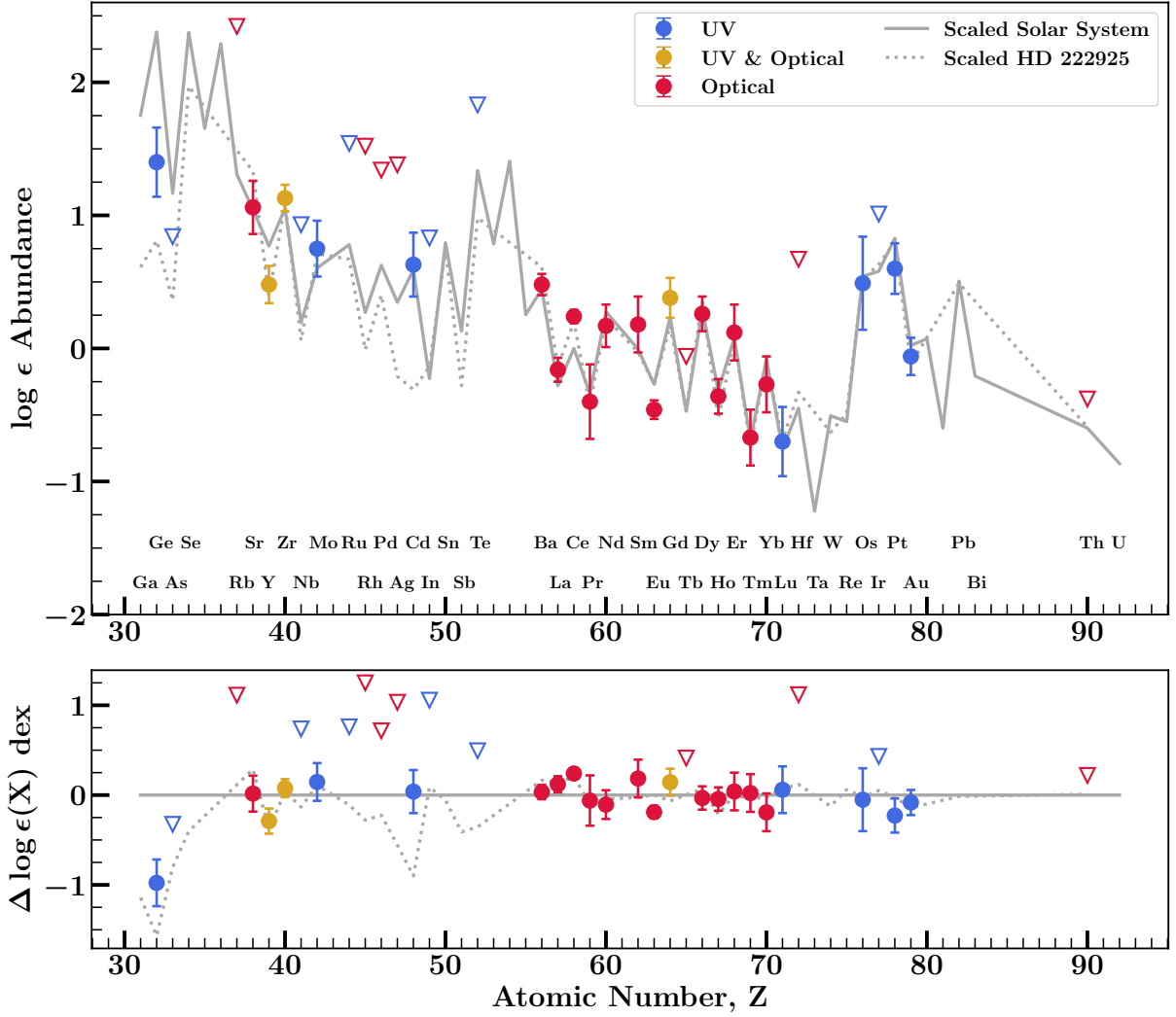


**Figure 4.** Adopted abundances of the  $r$ -process elements for J0051-1053 shown with different colored data points, depending on the wavelength-region used for deriving the abundance. Abundances obtained with the UV spectrum are shown in blue, with optical spectrum are shown in red, and with both UV and optical are shown in yellow. Upper limits are shown in downward-triangle with the same color map as the abundances. The grey-solid trace depicts the scaled S.S.  $r$ -process pattern as obtained from Prantzos et al. (2020). The grey-dotted line depicts the scaled  $r$ -process pattern of the RPE star, HD 222925, as obtained from Roederer et al. (2022a)

in the optical spectra, including Mg II, Al II, Co II, and Ni II. Additionally, since these are the dominant species, their detection enabled an empirical test of the NLTE effects affecting the corresponding neutral species of these elements (see Section 9.1.2).

The UV spectral coverage also benefited the abundance determinations of 14 species, increasing the number of absorption lines available. These species included Mg I, Si I, Si II, Sc II, Ti II, V II, Cr I, Cr II, Mn I, Mn II, Fe I, Fe II, Co I, and Ni I. We find that the optical and UV abundances of these species agree well, within uncertainties. This can be seen in the top panel of Figure 3, which shows the individual optical (black data) and UV (green data)  $[X/Fe]$  abundance ratio of each species. The agreement in the UV and optical abundances of these species validates our reduction and analysis techniques for the two spectra (e.g., Roederer et al. 2022b).

On the other hand, optical spectral coverage enabled us to determine abundances for 8 species which were not available

in the UV, including O I, Na I, Al I, K I, Ca I, Ti I, V I, and Zn I.

#### 9.1.2 Neutrals, Ions, and NLTE Effects

We obtained abundances of both the neutral and first-ionized species for several light elements. We plot these abundances as  $[X/Fe]$  abundance ratio in the middle panel of Figure 3, with square data points for neutral species and circular data points for first-ionized species. For this plot, we combined the UV and optical abundances of the species; both the UV and optical lines are considered for the mean  $[X/Fe]$  abundance ratio and the corresponding uncertainty of the species following the method described in Section 8. We also depict the LTE and NLTE-corrected abundances for each species separately, colored-coded with black and red data points, respectively.

As seen in Figure 3, the abundances of the neutral and

ionized species of most light elements agree. On the other hand, for HD 222925, [Roederer et al. \(2022a\)](#) observed that the abundances of the neutral species of Ca and Fe-group elements were all systematically lower than the abundances of their ionized counterparts. They noted that these offsets were consistent with over-ionization effects predicted for these species due to LTE assumptions. Given the higher  $\log g$  of J0051-1053, we suspect that the over-ionization effects are lower in this case and/or the precision of the abundances derived here is not sufficient to discern any systematic offset between the abundances of the neutral and ionized species.

We also find that the NLTE-corrected abundances of the neutral species (red-square points in the middle panel of Figure 3) generally agree well with the LTE abundances of the corresponding ionized species (black circular points). The agreement is very good for Mg and Si. In the cases of Mg I and Si I, the NLTE corrections are also small i.e., +0.10 dex and +0.00 dex, respectively. For Ti, Cr, Mn, and Fe, the agreement exists within uncertainties. We note that the NLTE corrections for Cr I (+0.25 dex), Mn I (+0.28 dex), and Fe I (+0.17 dex) are at least  $1\sigma$  higher than their respective uncertainties. Such significant corrections highlight the importance of NLTE studies and accounting for NLTE corrections as we move towards larger and more precise spectroscopic surveys and analyses. Overall, the general agreement between the NLTE-corrected abundances of the neutral species and the LTE abundances of the corresponding ionized species, in spite of the large corrections, reflects well on the current state of NLTE theoretical models for most species. Although, as spectroscopic studies start achieving higher precision in the abundances, discrepancies might be revealed.

An important exception to this case is Al, wherein the NLTE-corrected abundance of Al I and the LTE abundance of Al II are discrepant by  $\sim 0.4$  dex. The NLTE correction for the  $\lambda 3961$  Al I resonance line is significant and is estimated to be +0.47 dex by [Mashonkina et al. \(2016\)](#). We also used the NLTE grids from [Nordlander & Lind \(2017\)<sup>12</sup>](#), to obtain a similar correction of +0.49 dex. Other NLTE studies, such as [Lind et al. \(2022\)](#), suggest even smaller NLTE corrections for Al I, on the order of  $\sim 0.20$  dex. Interestingly, even with this significant correction, the NLTE-corrected abundance of Al I using the  $\lambda 3944$  and  $\lambda 3961$  resonance lines is still  $\sim 0.40$  dex smaller than the Al II LTE abundance with the  $\lambda 2669$  line. Moreover, [Mashonkina et al. \(2016\)](#) and [Nordlander & Lind \(2017\)](#) showed that NLTE effects for Al II are negligible. Therefore, for this study we adopted the Al II abundance. However, we recommend future NLTE studies to investigate the source of this discrepancy.

As noted in Section 6, for Li, O, Na, K, Ca, and Zn, we adopted the NLTE-corrected abundance of the neutral species (red square points in the middle panel of Figure 3), since the abundances of their ionized species were not available. The NLTE corrections for some of these elements are significant e.g.,  $-0.28$  dex for K I, +0.14 dex for Ca I, and +0.18 dex for Zn I (also see Table 1), indicating that it is especially important to take NLTE corrections into account for these elements, since their ionized species are generally not available. On the other hand, we note that the analysis of Zn I and Zn II abundances by [Roederer & Barklem \(2018\)](#)

for metal-poor dwarf and subgiant stars indicated minimal ( $\lesssim 0.10$  dex) departures from LTE.

### 9.1.3 Comparison to Other Metal-Poor Stars

We show the adopted light-element abundances of J0051-1053 in the bottom panel of Figure 3 with black data points and in the form of [X/Fe] abundance ratios. For comparison, we also display the typical values and range of the [X/Fe] abundance ratios for metal-poor stars. For this purpose, we used the light-element abundance ratios of 247 stars, as part of a sample of 313 stars analyzed by [Roederer et al. \(2014a\)](#). We obtained the abundances using JINAbase<sup>13</sup> ([Abohalima & Frebel 2018](#)). Specifically, we show the mean [X/Fe] abundance ratios of this sample with a grey-solid line and the  $\pm 1$  standard deviation from the mean with a shaded-grey region. As seen in the figure, we have obtained abundances of several light elements for J0051-1053.

The resulting [X/Fe] abundance ratios of J0051-1053 generally compare well with that of the metal-poor stars in the [Roederer et al. \(2014a\)](#) sample. Some discrepancies include [Al/Fe] and potentially [Ca/Fe], due to inconsistency in the adopted values. For [Al/Fe], we adopted the Al II abundance, which is much higher than the Al I abundance due to NLTE effects (see Section 9.1.2), whereas [Roederer et al. \(2014a\)](#) adopted the Al I abundance. Similarly, for [Ca/Fe], we adopted the NLTE-corrected Ca I abundance, while [Roederer et al. \(2014a\)](#) adopted the LTE Ca I abundance, which is generally slightly lower. We note that for O I, Na I, and K I, the NLTE-corrected abundances were adopted by both this study and [Roederer et al. \(2014a\)](#). Our final note is that for Ti, V, Cr, and Mn, both this study and [Roederer et al. \(2014a\)](#) adopted the abundance of the ionized species; on the other hand, for Mg, Si, and Co, we adopted the abundance of the ionized species and [Roederer et al. \(2014a\)](#) adopted the abundance of the neutral species, but no difference is observed in the abundance ratios.

In general, the trends in the light-element abundances of J0051-1053 compare well with that of other metal-poor stars, indicating that the primary enrichment channel for the light elements of J0051-1053 was core-collapse supernovae. We obtained an  $\alpha$ -enhancement of  $[\alpha/\text{Fe}] = +0.42$  for J0051-1053, using abundances of O, Na, Mg, Si, and Ca, which is typical of metal-poor stars ([Roederer et al. 2014a](#); [Cowan et al. 2020](#)). We included Ti as an iron-group element here, given the discussions in [Curtis et al. \(2019\)](#) and [Cowan et al. \(2020\)](#). The iron-group elements also exhibit the typical trends, including enhancement of Sc, Ti, and V, followed by solar ratios for Cr, Co, and Ni, followed by some enhancement for Zn ([Cowan et al. 2020](#); [Snedden et al. 2023](#)).

The elemental abundances not shown in Figure 3 are Li, CH, and CN. The Li abundance of  $\log \epsilon(\text{Li}) = 2.35$ , including the NLTE correction, falls along the Spite Plateau ([Spite & Spite 1982](#); [Norris et al. 2023](#)), which is expected for a turn-off star. Finally, with  $[\text{C}/\text{Fe}] = +0.62$ , using the CH abundance, we confirm that the star is not carbon enhanced. All in all, we determined abundances for 16 elements and one molecule (CH), and a  $3\sigma$  upper limit for one element (S) and one molecule (CN).

<sup>12</sup> <https://www.mso.anu.edu.au/~thomasn/NLTE/data/>

<sup>13</sup> <https://jinabase.pythonanywhere.com/index>

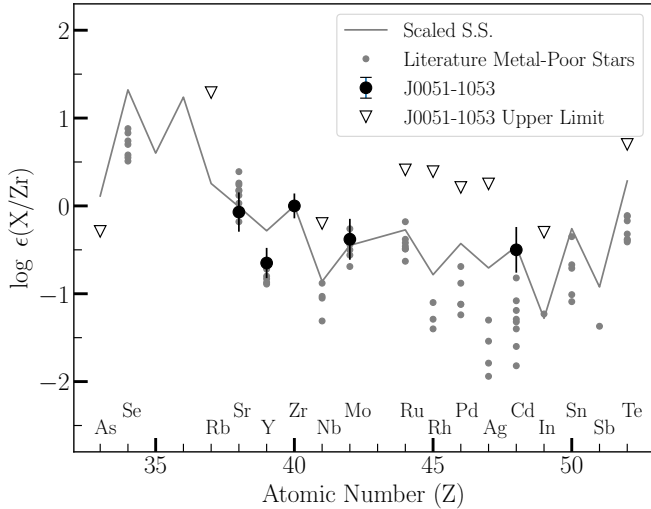


**Figure 5.** Light  $r$ -process elements of metal-poor stars scaled to Zr. As identified by Roederer et al. (2022b), abundances for Se, Sr, Y, Zr, Nb, Mo, and Te show minimal dispersion for the 8 metal-poor stars in their sample (grey data points). The S.S.  $r$ -process scaled to Zr is shown with a grey-solid line. We note that the scaled Sr, Y, and Mo abundances of J0051-1053 (black data points) follow the trend of other metal-poor stars. On the other hand, the scaled Cd abundance of J0051-1053 is much higher, the highest observed in metal-poor stars so far, adding to the observed dispersion of Cd abundances in metal-poor stars.

## 9.2 Heavy Elements and the $R$ -Process Pattern

We obtained abundances for 23  $r$ -process elements with  $31 \leq Z \leq 92$ . Out of these 23 elements, we obtained abundances of 8 elements with the UV spectrum and 3 elements with both the UV and optical spectrum. We also obtained  $3\sigma$  upper limits on the abundances of 13  $r$ -process elements. The UV spectrum especially enabled the upper limit determination for 6 of these elements.

We show the final abundances of all the neutron-capture elements in Figure 4. Given the  $r$ -process enhancement of the star as determined by  $[\text{Eu}/\text{Fe}] = +1.37$  and  $[\text{Ba}/\text{Eu}] = -0.72$  (Beers & Christlieb 2005; Frebel 2018), we confirm the findings of other studies (Ezzeddine et al. 2020; Gull et al. 2021) that J0051-1053 is an  $r$ -II star i.e., a highly  $r$ -process-enhanced star with  $[\text{Eu}/\text{Fe}] > +0.3$ . This classification is further affirmed by the abundance pattern of the neutron-capture elements, which generally matches the S.S.  $r$ -process pattern, as seen in Figure 4. Here the S.S.  $r$ -process pattern is scaled to the  $r$ -process pattern of J0051-1053 using the mean lanthanide abundance. For the mean lanthanide abundance, we specifically used abundances of elements from Ba to Hf, except for Sm and Tb, since we only have upper limits on their abundances. For comparison, we also show the abundance pattern of HD 222925, a metal-poor highly  $r$ -process-enhanced star with abundances of 42  $r$ -process elements determined by Roederer et al. (2018) and Roederer et al. (2022a). We note that the data points for J0051-1053 in the Figure 4 are color-coded based on the origin of the abundance of the elements from the UV spectrum (blue), optical (red), or both (yellow). We further discuss the  $r$ -process

pattern of J0051-1053 and compare it to the S.S. and HD 222925  $r$ -process patterns below.

### 9.2.1 $R$ -Process Pattern from the First to the Second $R$ -Process Peak

Various studies have indicated that the abundance pattern of the elements in this region (from  $Z = 31$  to  $Z = 52$ ) have a scatter and deviate from the S.S.  $r$ -process pattern, even in RPE stars (e.g., Siqueira Mello et al. 2014; Ji et al. 2016). The origin of this effect is still unknown, with different astrophysical sites, conditions, and processes being considered (e.g., Chiappini et al. 2011; Hansen et al. 2012; Wanajo 2013; Holmbeck et al. 2019). For J0051-1053, we also observe the Ge and Y abundances to be lower than the scaled S.S.  $r$ -process pattern (see Figure 4). Additionally, the upper limit on the As abundance is also significantly lower than the scaled S.S.  $r$ -process pattern. On the other hand, we observe the Sr, Zr, Mo, and Cd abundances to follow the scaled S.S.  $r$ -process pattern.

In the case of Ge, we find that its abundance ratio of  $[\text{Ge}/\text{Fe}] = +0.10$  is significantly higher than observed in  $\sim 20$  metal-poor stars so far, which have a mean  $[\text{Ge}/\text{Fe}]$  of  $\sim -0.90$  with a standard deviation of  $\sim 0.26$ , indicating a difference in the origin (Cowan et al. 2005; Roederer et al. 2014b; Peterson et al. 2020, and references therein). Cowan et al. (2005) showed that for metal-poor stars,  $[\text{Ge}/\text{H}]$  ratio is correlated with  $[\text{Fe}/\text{H}]$ , pointing to a common origin of Ge and Fe-peak elements, possibly  $\alpha$ -rich freezeout in core-collapse supernovae (also see Roederer et al. 2014b for a similar discussion and larger sample of abundances). However, other mechanisms are also capable of producing Ge, including the  $\nu p$ -process (e.g., Fröhlich et al. 2006) and the  $r$ -process (e.g., Farouqi et al. 2010), both of which have multiple potential astrophysical sites. Therefore, the high  $[\text{Ge}/\text{Fe}]$  ratio observed here may indicate a production mechanism of Ge decoupled from that of Fe. As noted by Roederer et al. (2014b), it will be challenging to establish the originating mechanism without the isotopic abundances. Nevertheless, this result renews the need for more Ge abundance determinations in metal-poor stars. We also consider that the Ge abundance derived here may not be dependable, since only one Ge I was used. Additionally, there could be NLTE effects present. Therefore, caution is warranted before over-interpreting this Ge abundance.

Interestingly, in a recent study, Roederer et al. (2022b) showed using 8 metal-poor stars, including 6 RPE, that the relative abundances of Se, Sr, Y, Zr, Nb, Mo, and Te in these stars actually all agree, provided that the abundances are scaled by a light  $r$ -process element. We find J0051-1053 to conform to this rule based on the derived abundances of Sr, Y, Zr, and Mo. We show this agreement in Figure 5, where we have plotted the Zr-scaled abundances of the Roederer et al. (2022b) sample stars with grey data points, and the Zr-scaled abundances of J0051-1053 with black data points. We also show the Zr-scaled  $r$ -process pattern of the S.S. from Prantzos et al. (2020) with a grey-solid line. Additionally, although we only have  $3\sigma$  upper limits for Nb and Te for J0051-1053, they don't rule out a possible agreement with other metal-poor stars. In fact, we note that the expected Te abundance, based on the Zr-scaled S.S.  $r$ -process pattern lends a stronger absorption signature for the Te I line than

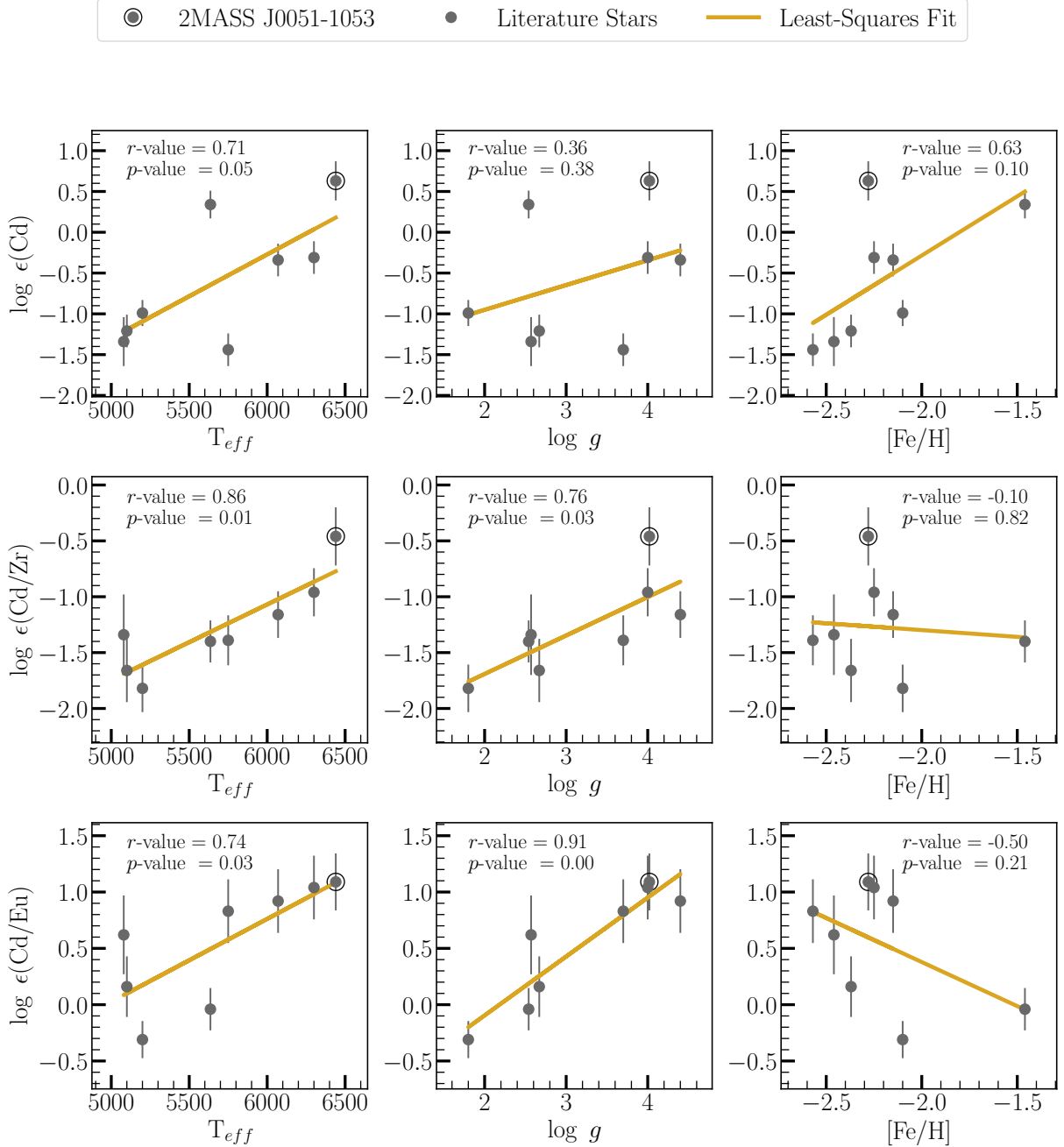


**Figure 6.** Cd abundances of J0051-1053 and other metal-poor stars (Roederer et al. 2022b, and references therein) with respect to stellar parameters of the stars, including  $T_{\text{eff}}$ ,  $\log g$ , and  $[\text{Fe}/\text{H}]$ . The absolute Cd abundances are shown in the top row, Cd abundance scaled to Zr are shown in the middle row, and Cd abundance scaled to Eu are shown in the bottom row. Also shown is the least-square fit to the data with a golden-solid line. The Pearson correlation coefficient ( $r$ -value) and the corresponding probability of observing a correlation of at least this magnitude by chance ( $p$ -value) are listed on the top for each panel.

the observed data suggests, indicating that the Zr-scaled Te abundance for J0051-1053 is not as high as the Zr-scaled S.S. Te abundance. On the other hand, the expected Te abundance, based on the Zr-scaled Te abundance of HD 222925 is more likely to be a better fit to the observed data. Therefore, our current results for J0051-1053 supports the hypothesis proposed by Roederer et al. (2022b) that the enrichment source of the light  $r$ -process elements in the early Universe

must have been common and consistent in producing the observed relative abundances of these elements.

We note here that several studies have pointed out the significant deviation of Y in metal-poor stars from the scaled S.S.  $r$ -process pattern (e.g., Sneden et al. 2003; Roederer et al. 2022b), as can be seen in Figures 4 and 5. A recent study by Storm & Bergemann (2023) computed NLTE departure coefficients for the low- and high-excitation Y II lines for a range of stellar parameters and found that these corrections



can be as large as +0.50 dex for low-excitation Y II lines in metal-poor red-giant stars. For a metal-poor turn-off star, they calculated NLTE corrections on the order of  $\sim +0.15$  dex for the low-excitation Y II lines. They proposed that such NLTE effects could contribute to the observed deviation of Y abundances from the S.S.  $r$ -process pattern. Indeed, we find that taking into account a +0.15 dex of NLTE effects for the low-excitation Y II lines used here would enable an agreement between the lanthanide-scaled Y abundance of J0051-1053 and the S.S.  $r$ -process pattern within uncertainties.

Although, as seen in Figure 5, such an agreement in the relative abundances of the light  $r$ -process elements in metal-poor stars does not extend to Ru, Rh, Pd, Ag, Cd, and Sn. Of these elements, for J0051-1053, we have abundance determined for Cd and  $3\sigma$  upper limits determined for Ru, Rh, Pd, and Ag. We find that J0051-1053 has the highest reported  $\log \epsilon(\text{Cd})$ ,  $\log \epsilon(\text{Cd}/\text{Zr})$  and  $\log \epsilon(\text{Cd}/\text{Eu})$  abundance among the 9 metal-poor stars with Cd abundance determined so far (Roederer et al. 2014b; Peterson et al. 2020; Roederer et al. 2022a, 2010b). This record-high abundance further contributes to the large dispersion in the  $\log \epsilon(\text{Cd}/\text{Zr})$  abundance ratio of metal-poor stars, as seen in Figure 5. Note that we have not included the Cd abundance of HD 196944 from Placco et al. (2015) in Figure 5, since its chemical composition mainly originates from the  $s$ -process.

While the production of Cd has not been of specific focus due to the small number of observations, theoretical studies have indicated that elements in this region ( $44 < Z < 51$ ) could be formed through the weak  $r$ -process i.e., a neutron-capture process with intermediate neutron densities (e.g., Montes et al. 2007). On the other hand, Vassh et al. (2020) showed that the elements in this region could also be products of late-time fissioning of heavy nuclei, which would also deposit material in the lanthanide region. In that case, the abundances of these elements would be correlated with heavier  $r$ -process elements like Eu, instead of other light  $r$ -process elements like Zr. Indeed, Roederer et al. (2023) observed correlations of Ru, Rh, Pd, and Ag abundances of  $r$ -process stars with their  $[\text{Eu}/\text{Fe}]$  ratios, supporting this theory and providing an explanation for the observed dispersion in the abundances of these elements when scaled with Zr, as seen in Figure 5. However, as shown by Roederer et al. (2023), Cd abundances of  $r$ -process stars do not show a similar correlation with  $[\text{Eu}/\text{Fe}]$ . We report here that this star adds to the evidence of a large dispersion in the Cd abundance, for which the cause continues to be unknown.

While the cause of such a dispersion of Cd abundances could be astrophysical, here we check for possible causes due to limitations in our stellar atmospheric models. For this purpose, we plot  $\log \epsilon(\text{Cd})$ ,  $\log \epsilon(\text{Cd}/\text{Zr})$ , and  $\log \epsilon(\text{Cd}/\text{Eu})$  abundances of all metal-poor stars with Cd abundance determined so far against their  $T_{\text{eff}}$ ,  $\log g$ , and  $[\text{Fe}/\text{H}]$  in Figure 6. The stars included are HD 128279 (Roederer et al. 2014b), HD 108317 (Roederer et al. 2014b), HD 140283 (Peterson et al. 2020), HD 19445 (Peterson et al. 2020), HD 84937 (Peterson et al. 2020), BD +17°3248 (Roederer et al. 2022b), and HD 222925 (Roederer et al. 2022a). We note that we only used Cd I abundances of these stars since these are typically the reported Cd abundances. We highlight the data points of J0051-1053 with a circular boundary around them.

We also fit the data with a linear least-square regression line, shown with golden-solid lines in Figure 6. We list

the Pearson correlation coefficient ( $r$ -value) and the corresponding  $p$ -value of the correlation in each panel. The  $r$ -value indicates the degree to which the two quantities are (anti-)correlated with  $(-1)+1$  indicating the strongest (anti-)correlation possible and 0 indicating no correlation. The  $p$ -value indicates the probability of a correlation equal to or stronger than what is observed, given the null hypothesis of no correlation. We find significant correlations ( $-0.5 < r$ -value  $< 0.5$  and  $p$ -value  $< 0.05$ ) of  $\log \epsilon(\text{Cd})$ ,  $\log \epsilon(\text{Cd}/\text{Zr})$ , and  $\log \epsilon(\text{Cd}/\text{Eu})$  with respect to  $T_{\text{eff}}$ , and of  $\log \epsilon(\text{Cd}/\text{Zr})$  and  $\log \epsilon(\text{Cd}/\text{Eu})$  abundances with respect to  $\log g$ . We find no significant correlation of any Cd-based abundances with respect to  $[\text{Fe}/\text{H}]$ .

Given the observed trends in the Cd abundance with respect to  $T_{\text{eff}}$  and  $\log g$ , we consider the case that the formation of the  $\lambda 2288$  Cd I line is strongly affected by NLTE. We note that Peterson et al. (2020) used Cd II and Cd I lines for 4 metal-poor stars. While they derived consistent abundances between the two species, they commented that the consistent abundances were only possible by ignoring the HFS of the Cd II, as reported in Roederer & Lawler (2012a). In the case that they used the HFS, inconsistent abundances were obtained. Such an inconsistency could further indicate strong NLTE effects for Cd I. With the present information, it is difficult to speculate the exact dependence of the NLTE effects on  $T_{\text{eff}}$  and  $\log g$ , if any, since their effects are degenerate. Therefore, we strongly urge the community to carry out detailed calculations to investigate the NLTE effects on Cd I abundances. We also encourage further theoretical investigations into a possible astrophysical origin for the dispersion in Cd abundances of metal-poor stars. Additional abundance determinations of Cd I and Cd II in metal-poor stars will also be helpful.

### 9.2.2 $R$ -Process Pattern from the Lanthanides to the Third $R$ -Process Peak

We find that, except for Ce and Eu, the  $r$ -process elements of J0051-1053 in the lanthanide region, from Ba ( $Z = 56$ ) to Lu ( $Z = 71$ ), adhere to the scaled  $r$ -process patterns of the S.S. and HD 222925. While the Ce abundance of J0051-1053 is higher than the scaled S.S.  $r$ -process abundance by 0.24 dex, it agrees well with the scaled Ce abundance of HD 222925. Since we are using only two weak Ce II lines, we believe that a higher resolution and S/N study is warranted to better understand this discrepancy with the scaled S.S. Ce abundance.

On the other hand, the Eu abundance of J0051-1053 is lower than the the scaled Eu abundances of both the S.S. and HD 222925 by  $\sim 0.18$  dex, which is more than  $1\sigma$ . Since we have used 5 Eu II lines, all of which are of intermediate strength and have been well-established in the literature, we find this Eu discrepancy of note. Typically, discrepancies between the Eu abundance of RPE stars and the S.S.  $r$ -process pattern are not discovered or reported, since the S.S.  $r$ -process patterns are often scaled relative to the Eu abundance of the stars. However, as noted previously, in this study we have scaled the  $r$ -process pattern of the S.S. and HD 222925 using the mean lanthanide abundance.

To understand this discrepancy, we consider the effects of NLTE on the formation of the Eu II lines. Zhao et al. (2016) estimated that for BD-04 3208, a dwarf metal-poor star with stellar parameters similar to J0051-1053 (Sitnova et al. 2015),

the Eu NLTE abundance was 0.13 dex higher than the LTE abundance, when using the  $\lambda 4129$  Eu II line. A similar NLTE correction for the mean Eu abundance of J0051-1053, which is within 0.01 dex of the  $\lambda 4129$  abundance, would enable an agreement of its Eu abundance with the scaled Eu abundances of the S.S. and HD 222295 within uncertainties.

While there have been several studies indicating that the universal  $r$ -process pattern extends to the third  $r$ -process peak (e.g., Cowan et al. 2005; Roederer et al. 2009; Barbuy et al. 2011; Roederer et al. 2022a), there have been only 5 RPE stars with a Au abundance determined (Cowan et al. 2002; Sneden et al. 2003; Barbuy et al. 2011; Roederer et al. 2012a, 2022a). Similarly, there have been only  $\sim 15$  RPE stars with a Pt abundance determined (Cowan et al. 1996; Westin et al. 2000; Cowan et al. 2002; Sneden et al. 2003; Cowan et al. 2005; Barbuy et al. 2011; Roederer et al. 2012a; Roederer & Lawler 2012b; Roederer et al. 2022a). Therefore, the Au and Pt abundances of J0051-1053 are highly valuable. Indeed, we find that our results on the abundances of these elements, along with that of Os, uphold the case for the extension of the universal  $r$ -process pattern to the third  $r$ -process peak and to Au.

We also find that, with  $[\text{Au}/\text{Fe}] = +1.37$ , J0051-1053 has the highest enhancement in gold discovered in any star thus far. However, we note that this enhancement is not substantially different from what is found in other stars, which have  $+0.80 < [\text{Au}/\text{Fe}] < +1.28$ . Such enhancements in Au ( $[\text{Au}/\text{Fe}] > 0.0$ ) remain at odds with the current Galactic chemical-enrichment models, which predict an underproduction of  $[\text{Au}/\text{Fe}]$  levels by a factor of 5, or by 0.80 dex (Kobayashi et al. 2020). It is possible that such a discrepancy exists due to the observational bias of having Au abundance determined for only a few stars, which are also RPE. Therefore, there is an urgent need for more abundance determination of Au in metal-poor stars, which will require access to high-resolution space-based observations in the UV. To that end, this study serves as an important contribution.

## 10 CONCLUSIONS

We have performed a detailed chemical-abundance analysis of a very metal-poor ( $[\text{Fe}/\text{H}] = -2.31$ ) turn-off RPE ( $[\text{Eu}/\text{Fe}] = 1.37$ ) star, 2MASS J00512646-1053170. For this, we obtained high-resolution HST/STIS and Magellan/MIKE spectroscopic data covering the UV ( $\sim 2275 - 3119 \text{ \AA}$ ) and optical (3350 - 9500  $\text{ \AA}$ ) wavelengths. J0051-1053 may be the warmest highly RPE star studied in both the UV and optical domains thus far. As a result of the wide wavelength coverage, we determined abundances for 41 elements in total. We have identified several key chemical signatures that contribute to our understanding of the origin of these elements, especially the  $r$ -process elements, and motivate future theoretical and observational studies.

- We determined abundances for 16 light elements, including 26 individual species. We found that the light elements follow the typical trends of metal-poor stars (bottom panel of Figure 3), indicating that their origin was primarily core-collapse supernovae.

- We found that the most significant NLTE corrections are for Al I, K I, Cr I, and Mn I abundances. We show the LTE

and NLTE-corrected abundances of individual species in the middle panel of Figure 3.

- We found that, even though the NLTE correction for Al I is large (+0.47 dex), it is still not sufficiently large to enable agreement with the LTE abundance of the dominant species, Al II, which remains  $\sim 0.4$  dex ( $\sim 2\sigma$ ) higher than the NLTE-corrected Al I abundance. Based on this result, we urge the community to investigate the NLTE effects for Al I and Al II further.

- Among the  $r$ -process elements, we determined detailed abundances for 23 elements and upper limits for 6 elements, ranging from the first  $r$ -process peak to the actinides (Figure 4). We found that J0051-1053, like many other RPE stars, exhibits variations in its pattern of light  $r$ -process-elements. Specifically, Ge and Y are found to deviate from the lanthanide-scaled S.S.  $r$ -process pattern. However, we find that taking into account NLTE effects for the low-excitation Y II lines would enable a better agreement with the S.S.  $r$ -process pattern. On the other hand, Sr, Y, Zr, and Mo follow the benchmark light  $r$ -process-pattern of metal-poor stars identified by Roederer et al. (2022b) (Figure 5), adding evidence for a common source of light  $r$ -process elements in the early Universe.

- We found that  $[\text{Ge}/\text{Fe}] = +0.10$  is significantly higher than observed in  $\sim 20$  metal-poor stars thus far, which exhibit  $[\text{Ge}/\text{Fe}] \sim -0.90$  with a standard deviation of  $\sim 0.28$  dex. The similar  $[\text{Ge}/\text{Fe}]$  ratios observed in metal-poor stars has indicated a common origin for Ge and Fe in the early Universe, for instance  $\alpha$ -rich freezeout. Therefore, the high  $[\text{Ge}/\text{Fe}]$  may indicate contribution from a production mechanism decoupled from that of Fe, such as the  $\nu p$ - or  $r$ -process.

- Similarly, the Cd abundance observed for this star is the highest to date, adding to the dispersion observed in the Cd abundances of metal-poor stars, which still remains unexplained (Figure 5). Here, we found that the  $\log \epsilon(\text{Cd})$ ,  $\log \epsilon(\text{Cd}/\text{Zr})$ , and  $\log \epsilon(\text{Cd}/\text{Eu})$  abundances of metal-poor stars are correlated to  $T_{\text{eff}}$  and  $\log g$  of the stars, suggesting that the Cd I line may be severely affected by NLTE effects, causing the observed dispersion (Figure 6). Therefore, we urge the community to theoretically study the NLTE effects for Cd I and Cd II, as well as revisit the astrophysical origin of this element.

- We found that the lanthanides generally follow the universal  $r$ -process-pattern. However, the Eu abundance was found to be mildly discrepant from the universal pattern, which we found explainable by NLTE effects.

- Additionally, the abundances of Os, Pt, and Au, uphold the case for the extension of the universal  $r$ -process-pattern to the third  $r$ -process peak (Figure 4) – while this case has been suggested by previous studies, it remains to be firmly established due to the scarce number of abundances of elements like Pt and Au.

- The abundance determination of Au marks J0051-1053 as only the 6th star with Au abundance determined. The enhancement in Au, relative to Fe, follows that of other metal-poor stars. These observed enhancements are five times higher than suggested by current Galactic chemical-evolution models, motivating the need for more abundance determinations of Au in metal-poor stars.

Overall, as part of the  $R$ -Process Alliance effort, this study adds to the sparse but growing number of RPE stars with

extensive and detailed inventory of chemical abundances. We anticipate more such studies with UV and optical spectroscopy in the near future, especially as an increasing number of  $r$ -process-enhanced stars are identified (e.g., Hansen et al. 2018; Sakari et al. 2018; Ezzeddine et al. 2020; Holmbeck et al. 2020). However, as highlighted in this study, it will also be necessary to advance the theoretical NLTE studies, especially of  $r$ -process elements, in concurrence with the astrophysical studies, which critically depend on the reliable abundance determination of these elements.

## ACKNOWLEDGEMENTS

This research is based on observations made with the NASA/ESA Hubble Space Telescope obtained from the Space Telescope Science Institute, which is operated by the Association of Universities for Research in Astronomy, Inc., under NASA contract NAS 5-26555. These observations are associated with program 15951. S.P.S acknowledges Jamie Tayar and Guilherme Limberg for helpful conversations. S.P.S and R.E. acknowledge support from NASA grant GO-15951 from the Space Telescope Science Institute, which is operated by the Association of Universities for Research in Astronomy, Inc., under NASA contract NAS5-26555. R.E acknowledges support NSF grant AST-2206263. I.U.R acknowledges NSF grants AST 1815403 and AST 2205847, NASA Astrophysics Data Analysis Program grant 80NSSC21K0627, as well as NASA grants GO-15657, GO-15951, and AR-16630 from the Space Telescope Science Institute, which is operated by the Association of Universities for Research in Astronomy, Incorporated, under NASA contract NAS5-26555. TTH acknowledges support from the Swedish Research Council (VR 2021-05556). The work of V.M.P. is supported by NOIRLab, which is managed by the Association of Universities for Research in Astronomy (AURA) under a cooperative agreement with the National Science Foundation. T.C.B. acknowledges partial support from grant PHY 14-30152; Physics Frontier Center/JINA Center for the Evolution of the Elements (JINA-CEE), and from OISE-1927130: The International Research Network for Nuclear Astrophysics (IReNA), awarded by the US National Science Foundation. A.P.J. acknowledges support from NSF grant AST-2206264. C.M.S acknowledges support from the NSF grant AST 2206379.

## DATA AVAILABILITY

The UV spectrum of 2MASS J00512646-1053170 is publicly available on the Mikulski Archive for Space Telescopes under the proposal ID 15951.

## REFERENCES

- Abomalima A., Frebel A., 2018, *ApJS*, **238**, 36
- Amarsi A. M., Asplund M., Collet R., Leenaarts J., 2016a, *MNRAS*, **455**, 3735
- Amarsi A. M., Lind K., Asplund M., Barklem P. S., Collet R., 2016b, *MNRAS*, **463**, 1518
- Arlandini C., Käppeler F., Wisshak K., Gallino R., Lugaro M., Busso M., Straniero O., 1999, *ApJ*, **525**, 886
- Asplund M., Grevesse N., Sauval A. J., Scott P., 2009, *ARA&A*, **47**, 481
- Bailer-Jones C. A. L., Rybizki J., Foesneau M., Demleitner M., Andrae R., 2021, *AJ*, **161**, 147
- Barbuy B., et al., 2011, *A&A*, **534**, A60
- Beers T. C., Christlieb N., 2005, *Annual Review of Astronomy and Astrophysics*, **43**, 531
- Beers T. C., et al., 2017, *ApJ*, **835**, 81
- Bergemann M., Cescutti G., 2010, *A&A*, **522**, A9
- Bergemann M., Pickering J. C., Gehren T., 2010, *MNRAS*, **401**, 1334
- Bergemann M., Kudritzki R.-P., Würl M., Plez B., Davies B., Gazak Z., 2013, *ApJ*, **764**, 115
- Bergemann M., et al., 2019, *A&A*, **631**, A80
- Bernstein R., Shectman S. A., Gunnels S. M., Mochnecki S., Athey A. E., 2003, in Iye M., Moorwood A. F. M., eds, *Society of Photo-Optical Instrumentation Engineers (SPIE) Conference Series Vol. 4841, Instrument Design and Performance for Optical/Infrared Ground-based Telescopes*. pp 1694–1704, doi:10.1117/12.461502
- Burbidge E. M., Burbidge G. R., Fowler W. A., Hoyle F., 1957, *Reviews of Modern Physics*, **29**, 547
- Cain M., et al., 2018, *ApJ*, **864**, 43
- Cameron A. G. W., 1957, *PASP*, **69**, 201
- Casagrande L., Vandenberg D. A., 2014, *MNRAS*, **444**, 392
- Casagrande L., Ramírez I., Meléndez J., Bessell M., Asplund M., 2010, *A&A*, **512**, A54
- Casey A. R., 2014, PhD thesis, Australian National University, Canberra
- Castelli F., Kurucz R. L., 2003, in Piskunov N., Weiss W. W., Gray D. F., eds, *Proceedings of the 210th Symposium of the International Astronomical Union Vol. 210, Modelling of Stellar Atmospheres*. p. A20 (arXiv:astro-ph/0405087)
- Cayrel R., 1988, in Cayrel de Strobel G., Spite M., eds, *Proceedings of the 132nd Symposium of the International Astronomical Union Vol. 132, The Impact of Very High S/N Spectroscopy on Stellar Physics*. p. 345
- Cayrel R., et al., 2001, *Nature*, **409**, 691
- Cayrel R., et al., 2004, *A&A*, **416**, 1117
- Chiappini C., Frischknecht U., Meynet G., Hirschi R., Barbuy B., Pignatari M., Decressin T., Maeder A., 2011, *Nature*, **472**, 454
- Cowan J. J., Sneden C., Truran J. W., Burris D. L., 1996, *ApJ*, **460**, L115
- Cowan J. J., et al., 2002, *ApJ*, **572**, 861
- Cowan J. J., et al., 2005, *ApJ*, **627**, 238
- Cowan J. J., Sneden C., Roederer I. U., Lawler J. E., Hartog E. A. D., Sobek J. S., Boesgaard A. M., 2020, *ApJ*, **890**, 119
- Cowan J. J., Sneden C., Lawler J. E., Aprahamian A., Wiescher M., Langanke K., Martínez-Pinedo G., Thielemann F.-K., 2021, *Reviews of Modern Physics*, **93**, 015002
- Curtis S., Ebinger K., Fröhlich C., Hempel M., Peregó A., Liebendörfer M., Thielemann F.-K., 2019, *ApJ*, **870**, 2
- Curtis S., Miller J. M., Fröhlich C., Sprouse T., Lloyd-Ronning N., Mumpower M., 2023, *ApJ*, **945**, L13
- Cutri R. M., et al., 2003, *VizieR Online Data Catalog*, p. II/246
- Delgado Mena E., Tsantaki M., Adibekyan V. Z., Sousa S. G., Santos N. C., González Hernández J. I., Israelian G., 2017, *A&A*, **606**, A94
- Den Hartog E. A., Herd M. T., Lawler J. E., Sneden C., Cowan J. J., Beers T. C., 2005, *ApJ*, **619**, 639
- Den Hartog E. A., Lawler J. E., Roederer I. U., 2020, *ApJS*, **248**, 10
- Den Hartog E. A., Lawler J. E., Roederer I. U., 2021, *ApJS*, **254**, 5
- Eichler M., et al., 2016, in *Journal of Physics Conference Series*. p. 012054, doi:10.1088/1742-6596/665/1/012054
- Ezzeddine R., Frebel A., Plez B., 2017, *ApJ*, **847**, 142
- Ezzeddine R., et al., 2020, *ApJ*, **898**, 150

- Farouqi K., Kratz K. L., Pfeiffer B., Rauscher T., Thielemann F. K., Truran J. W., 2010, *ApJ*, **712**, 1359
- François P., et al., 2007, *A&A*, **476**, 935
- Frebel A., 2018, *Annual Review of Nuclear and Particle Science*, **68**, 237
- Frebel A., et al., 2006, *ApJ*, **652**, 1585
- Frebel A., Casey A. R., Jacobson H. R., Yu Q., 2013, *ApJ*, **769**, 57
- Fröhlich C., Martínez-Pinedo G., Liebendörfer M., Thielemann F. K., Bravo E., Hix W. R., Langanke K., Zimmer N. T., 2006, *Phys. Rev. Lett.*, **96**, 142502
- Goriely S., Arnould M., 2001, *A&A*, **379**, 1113
- Gull M., Frebel A., Hinojosa K., Roederer I. U., Ji A. P., Brauer K., 2021, *ApJ*, **912**, 52
- Hannaford P., Larkins P. L., Lowe R. M., 1981, *Journal of Physics B Atomic Molecular Physics*, **14**, 2321
- Hansen C. J., et al., 2012, *A&A*, **545**, A31
- Hansen T. T., et al., 2018, *ApJ*, **858**, 92
- Hansen T. T., et al., 2019, Testing r-process nucleosynthesis models with two r-process enhanced stars, HST Proposal. Cycle 27, ID. #15951
- Hansen T. T., et al., 2021, *ApJ*, **915**, 103
- Henden A., Munari U., 2014, Contributions of the Astronomical Observatory Skalnate Pleso, **43**, 518
- Hill V., et al., 2002, *A&A*, **387**, 560
- Hinkle K., Wallace L., Valenti J., Harmer D., 2000, Visible and Near Infrared Atlas of the Arcturus Spectrum 3727-9300 A
- Holmbeck E. M., Frebel A., McLaughlin G. C., Mumpower M. R., Sprouse T. M., Surman R., 2019, *ApJ*, **881**, 5
- Holmbeck E. M., et al., 2020, *ApJS*, **249**, 30
- Holmbeck E. M., Surman R., Roederer I. U., McLaughlin G. C., Frebel A., 2023, *ApJ*, **951**, 30
- Ivarsson S., Wahlgren G. M., Dai Z., Lundberg H., Leckrone D. S., 2004, *A&A*, **425**, 353
- Ji A. P., Frebel A., Simon J. D., Chiti A., 2016, *ApJ*, **830**, 93
- Ji A. P., et al., 2020, *AJ*, **160**, 181
- Ji A. P., Naidu R. P., Brauer K., Ting Y.-S., Simon J. D., 2022, arXiv e-prints, p. [arXiv:2207.04016](https://arxiv.org/abs/2207.04016)
- Keeping E., 1962, Introduction to Statistical Inference. Princeton, NJ: Van Nostrand-Reinhold
- Kelson D. D., 2003, *PASP*, **115**, 688
- Kelson D. D., Illingworth G. D., van Dokkum P. G., Franx M., 2000, *ApJ*, **531**, 159
- Kimble R. A., et al., 1998, *ApJ*, **492**, L83
- Kobayashi C., Karakas A. I., Lugaro M., 2020, *ApJ*, **900**, 179
- Koppelman H. H., Helmi A., Massari D., Roelenga S., Bastian U., 2019, *A&A*, **625**, A5
- Kowkabay J., et al., 2022, arXiv e-prints, p. [arXiv:2209.02184](https://arxiv.org/abs/2209.02184)
- Kramida A., Yu. Ralchenko Reader J., and NIST ASD Team 2022, NIST Atomic Spectra Database (ver. 5.10), [Online]. Available: <https://physics.nist.gov/asd> [2016, January 31]. National Institute of Standards and Technology, Gaithersburg, MD.
- Limberg G., et al., 2021, *ApJ*, **913**, L28
- Lind K., Melendez J., Asplund M., Collet R., Magic Z., 2013, *A&A*, **554**, A96
- Lind K., et al., 2022, *A&A*, **665**, A33
- Lippuner J., Fernández R., Roberts L. F., Foucart F., Kasen D., Metzger B. D., Ott C. D., 2017, *MNRAS*, **472**, 904
- Marshall J. L., et al., 2019, *ApJ*, **882**, 177
- Mashonkina L. I., Belyaev A. K., Shi J. R., 2016, *Astronomy Letters*, **42**, 366
- Mashonkina L., Sitnova T., Belyaev A. K., 2017, *A&A*, **605**, A53
- Masseron T., et al., 2014, *A&A*, **571**, A47
- McCall M. L., 2004, *AJ*, **128**, 2144
- Montes F., et al., 2007, *ApJ*, **671**, 1685
- National Academies of Sciences E., Medicine 2021, Pathways to Discovery in Astronomy and Astrophysics for the 2020s, [doi:10.17226/26141](https://doi.org/10.17226/26141).
- Nordlander T., Lind K., 2017, *A&A*, **607**, A75
- Norris J. E., Yong D., Frebel A., Ryan S. G., 2023, *MNRAS*, **522**, 1358
- Peterson R. C., 2011, *ApJ*, **742**, 21
- Peterson R. C., Barbuy B., Spite M., 2020, *A&A*, **638**, A64
- Placco V. M., Frebel A., Beers T. C., Stancliffe R. J., 2014, *ApJ*, **797**, 21
- Placco V. M., et al., 2015, *ApJ*, **812**, 109
- Placco V. M., et al., 2020, *ApJ*, **897**, 78
- Placco V. M., Sneden C., Roederer I. U., Lawler J. E., Den Hartog E. A., Hejazi N., Maas Z., Bernath P., 2021a, linemake: Line list generator, Astrophysics Source Code Library, record ascl:2104.027 (ascl:2104.027)
- Placco V. M., Sneden C., Roederer I. U., Lawler J. E., Den Hartog E. A., Hejazi N., Maas Z., Bernath P., 2021b, *Research Notes of the American Astronomical Society*, **5**, 92
- Plez B., et al., 2004, *A&A*, **428**, L9
- Prantzos N., 2012, *A&A*, **542**, A67
- Prantzos N., Abia C., Cristallo S., Limongi M., Chieffi A., 2020, *MNRAS*, **491**, 1832
- Quinet P., Palmeri P., Biémont É., Jorissen A., van Eck S., Svanberg S., Xu H. L., Plez B., 2006, *A&A*, **448**, 1207
- Roederer I. U., Barklem P. S., 2018, *ApJ*, **857**, 2
- Roederer I. U., Lawler J. E., 2012a, *ApJ*, **750**, 76
- Roederer I. U., Lawler J. E., 2012b, *ApJ*, **750**, 76
- Roederer I. U., Lawler J. E., 2021, *ApJ*, **912**, 119
- Roederer I. U., Kratz K.-L., Frebel A., Christlieb N., Pfeiffer B., Cowan J. J., Sneden C., 2009, *ApJ*, **698**, 1963
- Roederer I. U., Sneden C., Thompson I. B., Preston G. W., Shectman S. A., 2010a, *ApJ*, **711**, 573
- Roederer I. U., Sneden C., Lawler J. E., Cowan J. J., 2010b, *ApJ*, **714**, L123
- Roederer I. U., et al., 2012a, *ApJS*, **203**, 27
- Roederer I. U., et al., 2012b, *ApJ*, **747**, L8
- Roederer I. U., Preston G. W., Thompson I. B., Shectman S. A., Sneden C., Burley G. S., Kelson D. D., 2014a, *AJ*, **147**, 136
- Roederer I. U., et al., 2014b, *ApJ*, **791**, 32
- Roederer I. U., Placco V. M., Beers T. C., 2016, *ApJ*, **824**, L19
- Roederer I. U., Sakari C. M., Placco V. M., Beers T. C., Ezzeddine R., Frebel A., Hansen T. T., 2018, *ApJ*, **865**, 129
- Roederer I. U., et al., 2022a, *ApJS*, **260**, 27
- Roederer I. U., et al., 2022b, *ApJ*, **936**, 84
- Roederer I. U., et al., 2023, *Science*, **382**, 1177
- Sakari C. M., et al., 2018, *ApJ*, **868**, 110
- Schatz H., Toenjes R., Pfeiffer B., Beers T. C., Cowan J. J., Hill V., Kratz K.-L., 2002, *ApJ*, **579**, 626
- Schlafly E. F., Finkbeiner D. P., 2011, *ApJ*, **737**, 103
- Shah S. P., et al., 2023, *ApJ*, **948**, 122
- Siegel D. M., Barnes J., Metzger B. D., 2019, *Nature*, **569**, 241
- Siqueira Mello C., et al., 2013, *A&A*, **550**, A122
- Siqueira Mello C., et al., 2014, *A&A*, **565**, A93
- Sitnova T., et al., 2015, *ApJ*, **808**, 148
- Sitnova T. M., Yakovleva S. A., Belyaev A. K., Mashonkina L. I., 2020, *Astronomy Letters*, **46**, 120
- Sitnova T. M., Yakovleva S. A., Belyaev A. K., Mashonkina L. I., 2022, *MNRAS*, **515**, 1510
- Sneden C. A., 1973, PhD thesis, University of Texas, Austin
- Sneden C., Cowan J. J., Burris D. L., Truran J. W., 1998, *ApJ*, **496**, 235
- Sneden C., Cowan J. J., Ivans I. I., Fuller G. M., Burles S., Beers T. C., Lawler J. E., 2000, *ApJ*, **533**, L139
- Sneden C., et al., 2003, *ApJ*, **591**, 936
- Sneden C., Cowan J. J., Gallino R., 2008, *ARA&A*, **46**, 241
- Sneden C., Lawler J. E., Cowan J. J., Ivans I. I., Den Hartog E. A., 2009, *ApJS*, **182**, 80
- Sneden C., Boesgaard A. M., Cowan J. J., Roederer I. U., Den Hartog E. A., Lawler J. E., 2023, arXiv e-prints, p. [arXiv:2304.06899](https://arxiv.org/abs/2304.06899)
- Sobeck J. S., et al., 2011, *AJ*, **141**, 175

- Spite F., Spite M., 1982, *A&A*, [115](#), 357
- Storm N., Bergemann M., 2023, *MNRAS*, [525](#), 3718
- Takeda Y., Zhao G., Chen Y.-Q., Qiu H.-M., Takada-Hidai M., 2002, *PASJ*, [54](#), 275
- Thévenin F., Idiart T. P., 1999, *ApJ*, [521](#), 753
- Vassh N., et al., 2019, *Journal of Physics G Nuclear Physics*, [46](#), 065202
- Vassh N., Mumpower M. R., McLaughlin G. C., Sprouse T. M., Surman R., 2020, *ApJ*, [896](#), 28
- Venn K. A., Irwin M., Shetrone M. D., Tout C. A., Hill V., Tolstoy E., 2004, *AJ*, [128](#), 1177
- Wanajo S., 2013, *ApJ*, [770](#), L22
- Wang E. X., Nordlander T., Asplund M., Amarsi A. M., Lind K., Zhou Y., 2021, *MNRAS*, [500](#), 2159
- Westin J., Sneden C., Gustafsson B., Cowan J. J., 2000, *ApJ*, [530](#), 783
- Woodgate B. E., et al., 1998, *PASP*, [110](#), 1183
- Zhang M., Zhou L., Gao Y., Yu Q., Wang X., Wang Q., Gong Y., Dai Z., 2018, *Journal of Physics B Atomic Molecular Physics*, [51](#), 205001
- Zhao G., et al., 2016, *ApJ*, [833](#), 225

## APPENDIX A: LINELIST

Species	Wavelength (Å)	$\chi$ (eV)	$\log gf$	Type	$\log \epsilon(X)$	$\sigma_{sys}$
LiI	6707.8	0.0	0.17	syn	2.37	0.05
OI	7771.94	9.15	0.37	syn	7.12	0.05
OI	7774.17	9.15	0.22	syn	7.09	0.05
OI	7775.39	9.15	0.00	syn	7.04	0.05
NaI	5889.95	0.0	0.11	eqw	4.03	0.09
NaI	5895.92	0.0	-0.19	eqw	3.92	0.07
NaI	8183.26	2.1	0.24	eqw	3.93	0.03
NaI	8194.81	2.1	0.54	eqw	4.07	0.03
MgI	2736.54	2.72	-1.01	syn	5.64	0.05
MgI	2936.74	2.71	-2.27	syn	5.68	0.06
MgI	4057.51	4.35	-0.90	syn	5.85	0.02
MgI	4167.27	4.35	-0.74	syn	5.88	0.02
MgI	4571.1	0.0	-5.62	syn	5.72	0.07
MgI	4702.99	4.35	-0.44	syn	5.75	0.03
MgI	5172.68	2.71	-0.36	syn	5.64	0.08
MgI	5183.60	2.72	-0.17	syn	5.63	0.09
MgI	5528.4	4.35	-0.55	syn	5.65	0.03
MgII	2928.63	4.42	-0.53	syn	5.7	0.08
AlI	3943.0	0.0	-0.64	syn	3.42	0.07
AlI	3961.52	0.01	-0.33	syn	3.23	0.06
AlIII	2669.16	0.0	-4.98	syn	4.18	0.06
SiI	2987.64	0.78	-1.97	syn	5.58	0.08
SiI	3905.52	1.91	-1.04	syn	5.53	0.1
SiIII	2334.41	0.0	-5.09	syn	5.59	0.05
SiIII	2350.17	0.04	-5.12	syn	5.6	0.07
SiII	6371.36	8.12	-0.08	syn	5.47	0.04
SI	6757.13	7.87	-0.13	syn	<5.98	-
KI	7698.96	0.0	-0.18	eqw	3.33	0.05
CaI	4226.74	0.0	0.24	eqw	4.36	0.11
CaI	4283.01	1.89	-0.2	eqw	4.4	0.05
CaI	4318.65	1.9	-0.21	eqw	4.34	0.05
CaI	4425.44	1.88	-0.41	eqw	4.49	0.05
CaI	4434.96	1.89	-0.06	eqw	4.43	0.05
CaI	4435.69	1.89	-0.55	eqw	4.56	0.04
CaI	4454.78	1.9	0.26	eqw	4.35	0.05
CaI	4455.89	1.9	-0.55	eqw	4.46	0.05
CaI	4578.55	2.52	-0.67	eqw	4.58	0.04
CaI	5261.71	2.52	-0.6	eqw	4.61	0.04
CaI	5512.98	2.93	-0.45	eqw	4.59	0.03
CaI	5581.97	2.52	-0.58	eqw	4.49	0.04
CaI	5588.76	2.52	0.3	eqw	4.43	0.04
CaI	5590.12	2.52	-0.6	eqw	4.58	0.04
CaI	5857.45	2.93	0.17	eqw	4.5	0.03
CaI	6102.72	1.88	-0.81	eqw	4.39	0.05
CaI	6122.22	1.89	-0.33	eqw	4.46	0.05
CaI	6162.17	1.9	-0.11	eqw	4.46	0.05
CaI	6169.06	2.52	-0.87	eqw	4.62	0.04
CaI	6169.56	2.53	-0.6	eqw	4.6	0.04
CaI	6439.07	2.52	0.33	eqw	4.45	0.04
CaI	6449.81	2.52	-0.55	eqw	4.52	0.04
CaI	6499.65	2.52	-0.81	eqw	4.31	0.04
CaI	6717.69	2.71	-0.58	eqw	4.46	0.04
ScII	2551.0	-	-	syn	1.13	0.04
ScII	3572.53	0.02	0.27	syn	1.17	0.09
ScII	3576.34	0.01	0.01	syn	1.13	0.09
ScII	3590.47	0.02	-0.55	syn	1.1	0.04
ScII	3630.74	0.01	0.22	syn	0.99	0.05
ScII	4246.81	0.32	0.24	syn	1.15	0.05

ScII	4314.08	0.62	-0.1	syn	1.14	0.02
ScII	4320.73	0.6	-0.25	syn	1.1	0.04
ScII	4324.98	0.59	-0.44	syn	1.02	0.04
ScII	4374.45	0.62	-0.42	syn	1.12	0.03
ScII	4400.38	0.6	-0.54	syn	1.09	0.04
ScII	4415.54	0.59	-0.67	syn	1.03	0.04
ScII	4670.4	1.36	-0.58	syn	1.15	0.04
TiI	3989.76	0.02	-0.13	eqw	3.18	0.07
TiI	3998.64	0.05	0.02	eqw	3.13	0.07
TiI	4512.73	0.84	-0.4	eqw	3.29	0.06
TiI	4518.02	0.83	-0.25	eqw	3.19	0.06
TiI	4533.24	0.85	0.54	eqw	3.1	0.06
TiI	4534.78	0.84	0.35	eqw	3.1	0.06
TiI	4681.91	0.05	-1.01	eqw	3.38	0.07
TiI	4981.73	0.84	0.57	eqw	3.05	0.06
TiI	4991.07	0.84	0.45	eqw	3.13	0.06
TiI	4999.5	0.83	0.32	eqw	3.22	0.06
TiI	5173.74	0.0	-1.06	eqw	3.36	0.07
TiI	5192.97	0.02	-0.95	eqw	3.31	0.07
TiII	2761.29	1.08	-1.35	syn	3.0	0.07
TiII	2841.93	0.61	-0.59	syn	3.18	0.09
TiII	3029.73	1.57	-0.35	syn	3.04	0.04
TiII	3048.76	1.58	-1.18	syn	3.2	0.07
TiII	3340.34	0.11	-0.53	eqw	3.26	0.18
TiII	3343.76	0.15	-1.18	eqw	3.03	0.11
TiII	3372.79	0.01	0.28	eqw	3.48	0.14
TiII	3387.83	0.03	-0.41	eqw	3.46	0.19
TiII	3456.38	2.06	-0.11	eqw	2.65	0.04
TiII	3477.18	0.12	-0.95	eqw	3.36	0.17
TiII	3489.74	0.14	-2.0	eqw	3.21	0.07
TiII	3491.05	0.11	-1.1	eqw	3.22	0.14
TiII	3759.29	0.61	0.28	eqw	3.13	0.17
TiII	3761.32	0.57	0.18	eqw	3.06	0.17
TiII	3913.46	1.12	-0.36	eqw	3.03	0.09
TiII	4028.34	1.89	-0.92	eqw	3.08	0.03
TiII	4394.06	1.22	-1.77	eqw	3.1	0.04
TiII	4395.03	1.08	-0.54	eqw	3.13	0.09
TiII	4395.84	1.24	-1.93	eqw	3.09	0.04
TiII	4399.77	1.24	-1.2	eqw	3.06	0.04
TiII	4417.71	1.17	-1.19	eqw	3.06	0.04
TiII	4418.33	1.24	-1.99	eqw	3.17	0.04
TiII	4443.8	1.08	-0.71	eqw	3.09	0.07
TiII	4444.55	1.12	-2.2	eqw	3.04	0.04
TiII	4450.48	1.08	-1.52	eqw	3.1	0.04
TiII	4464.45	1.16	-1.81	eqw	3.08	0.04
TiII	4470.85	1.17	-2.02	eqw	2.89	0.04
TiII	4501.27	1.12	-0.77	eqw	3.12	0.07
TiII	4533.96	1.24	-0.53	eqw	3.06	0.07
TiII	4571.97	1.57	-0.31	eqw	3.07	0.06
TiII	4657.2	1.24	-2.29	eqw	3.08	0.04
TiII	4708.66	1.24	-2.35	eqw	3.16	0.04
TiII	4798.53	1.08	-2.66	eqw	3.17	0.04
TiII	5188.69	1.58	-1.05	eqw	3.12	0.04
TiII	5226.54	1.57	-1.26	eqw	3.07	0.04
TiII	5336.79	1.58	-1.6	eqw	3.01	0.04
TiII	5381.02	1.57	-1.97	eqw	3.16	0.04
TiII	5418.77	1.58	-2.13	eqw	3.32	0.04
VI	4111.78	0.3	0.4	syn	2.05	0.1
VII	2679.32	0.03	-0.63	syn	1.96	0.05
VII	2688.71	0.04	-0.98	syn	2.02	0.09
VII	2700.93	0.04	-0.37	syn	2.05	0.05
VII	2707.86	0.0	-1.39	syn	2.11	0.13

VII	2880.03	0.35	-0.64	syn	1.9	0.1
VII	2903.07	0.32	-0.7	syn	1.89	0.05
VII	3517.3	1.13	-0.24	syn	1.89	0.03
VII	3545.2	1.09	-0.32	syn	2.05	0.02
VII	3715.46	1.57	-0.22	syn	2.0	0.04
VII	3727.34	1.69	-0.23	syn	1.95	0.04
VII	3903.25	1.48	-0.91	syn	1.98	0.08
VII	4005.7	1.82	-0.45	syn	1.92	0.04
VII	4023.38	1.8	-0.61	syn	2.03	0.03
CrI	3015.2	0.96	-0.2	syn	3.23	0.07
CrI	3021.56	1.03	0.61	syn	3.2	0.2
CrI	3908.76	1.0	-1.05	syn	3.42	0.06
CrI	4616.12	0.98	-1.19	syn	3.4	0.02
CrI	4646.16	1.03	-0.74	syn	3.3	0.05
CrI	4652.16	1.0	-1.04	syn	3.31	0.04
CrI	5206.04	0.94	0.02	syn	3.29	0.08
CrI	5345.8	1.0	-0.95	syn	3.3	0.06
CrII	2666.01	1.51	-0.08	syn	3.44	0.05
CrII	2668.71	1.49	-0.55	syn	3.42	0.0
CrII	2671.81	1.51	-0.38	syn	3.51	0.08
CrII	2677.16	1.55	0.35	syn	3.51	0.07
CrII	2687.09	1.51	-0.62	syn	3.5	0.02
CrII	2751.87	1.53	-0.29	syn	3.51	0.2
CrII	2856.76	2.43	-0.59	syn	3.44	0.12
CrII	2865.33	2.42	-0.71	syn	3.52	0.06
CrII	2867.09	2.43	-0.5	syn	3.42	0.07
CrII	2876.24	1.51	-0.87	syn	3.39	0.05
CrII	2878.45	1.55	-1.27	syn	3.38	0.07
CrII	3408.77	2.48	-0.27	syn	3.3	0.07
CrII	4588.2	4.07	-0.65	syn	3.31	0.02
CrII	4618.81	4.07	-0.89	syn	3.33	0.03
MnI	2298.84	2.89	-1.75	syn	3.12	0.01
MnI	2610.51	3.07	-0.28	syn	2.8	0.11
MnI	2706.14	2.95	-1.34	syn	2.75	0.06
MnI	4041.35	2.11	0.28	syn	2.78	0.03
MnI	4055.54	2.14	-0.08	syn	2.82	0.11
MnI	4754.04	2.28	-0.08	syn	2.8	0.06
MnI	4762.37	2.89	0.3	syn	2.83	0.04
MnI	4783.43	2.3	0.04	syn	2.83	0.04
MnII	2939.31	1.17	0.11	syn	3.05	0.03
MnII	2949.20	1.18	0.25	syn	2.89	0.06
MnII	3441.99	1.78	-0.35	syn	2.87	0.03
MnII	3460.32	1.81	-0.63	syn	2.87	0.07
MnII	3482.90	1.83	-0.84	syn	2.97	0.07
MnII	3488.68	1.85	-0.94	syn	2.82	0.05
FeI	2283.66	0.11	-2.22	syn	5.23	0.1
FeI	2294.41	0.11	-1.54	syn	5.25	0.04
FeI	2485.99	0.92	-1.61	syn	5.14	0.1
FeI	2539.36	0.92	-1.79	syn	5.2	0.1
FeI	2636.48	0.92	-2.04	syn	5.3	0.08
FeI	2641.64	0.92	-1.32	syn	4.95	0.05
FeI	2644.0	1.01	-0.91	syn	4.94	0.05
FeI	2645.42	0.11	-2.75	syn	5.02	0.05
FeI	2647.56	0.05	-2.42	syn	5.25	0.07
FeI	2666.4	0.96	-1.87	syn	5.2	0.07
FeI	2680.45	0.99	-1.74	syn	4.95	0.05
FeI	2690.07	0.0	-2.72	syn	5.12	0.04
FeI	2728.02	0.92	-1.46	syn	5.16	0.09
FeI	2730.98	1.01	-1.73	syn	5.18	0.11
FeI	2838.12	0.99	-1.11	syn	5.18	0.06
FeI	2877.3	1.48	-1.3	syn	5.16	0.03
FeI	2960.66	2.95	-1.0	syn	5.2	0.09



FeI	2966.9	0.0	-0.4	syn	5.31	0.11
FeI	3009.57	0.92	-0.76	syn	5.25	0.1
FeI	3024.03	0.11	-1.48	syn	5.23	0.16
FeI	3059.09	0.05	-0.69	syn	5.1	0.06
FeI	3406.8	2.22	-0.96	eqw	5.21	0.08
FeI	3440.61	0.0	-0.67	eqw	5.27	0.19
FeI	3440.99	0.05	-0.96	eqw	5.43	0.2
FeI	3451.91	2.22	-1.0	eqw	5.17	0.07
FeI	3490.57	0.05	-1.1	eqw	5.36	0.2
FeI	3540.12	2.87	-0.71	eqw	5.14	0.07
FeI	3565.38	0.96	-0.13	eqw	5.38	0.18
FeI	3608.86	1.01	-0.09	eqw	5.35	0.18
FeI	3618.77	0.99	-0.0	eqw	5.22	0.18
FeI	3647.84	0.92	-0.14	eqw	4.93	0.16
FeI	3727.62	0.96	-0.61	eqw	5.08	0.15
FeI	3742.62	2.94	-0.81	eqw	5.06	0.05
FeI	3758.23	0.96	-0.01	eqw	5.05	0.15
FeI	3786.68	1.01	-2.18	eqw	5.18	0.07
FeI	3787.88	1.01	-0.84	eqw	5.12	0.13
FeI	3815.84	1.48	0.24	eqw	5.08	0.15
FeI	3849.97	1.01	-0.86	eqw	5.21	0.14
FeI	3856.37	0.05	-1.28	eqw	5.27	0.18
FeI	3865.52	1.01	-0.95	eqw	5.17	0.13
FeI	3878.02	0.96	-0.9	eqw	5.22	0.14
FeI	3899.71	0.09	-1.52	eqw	5.25	0.16
FeI	3902.95	1.56	-0.44	eqw	5.07	0.12
FeI	3920.26	0.12	-1.73	eqw	5.32	0.15
FeI	3922.91	0.05	-1.63	eqw	5.35	0.17
FeI	3949.95	2.18	-1.25	eqw	5.22	0.06
FeI	3977.74	2.2	-1.12	eqw	5.12	0.06
FeI	4005.24	1.56	-0.58	eqw	5.12	0.11
FeI	4045.81	1.49	0.28	eqw	5.18	0.14
FeI	4058.22	3.21	-1.18	eqw	5.39	0.05
FeI	4063.59	1.56	0.06	eqw	5.21	0.15
FeI	4067.98	3.21	-0.53	eqw	5.28	0.05
FeI	4070.77	3.24	-0.87	eqw	5.36	0.05
FeI	4071.74	1.61	-0.01	eqw	5.16	0.14
FeI	4114.44	2.83	-1.3	eqw	4.97	0.05
FeI	4132.06	1.61	-0.68	eqw	5.26	0.11
FeI	4134.68	2.83	-0.65	eqw	5.21	0.05
FeI	4143.87	1.56	-0.51	eqw	5.16	0.12
FeI	4147.67	1.49	-2.07	eqw	5.26	0.07
FeI	4154.5	2.83	-0.69	eqw	5.13	0.05
FeI	4156.8	2.83	-0.81	eqw	5.21	0.05
FeI	4157.78	3.42	-0.4	eqw	5.14	0.05
FeI	4174.91	0.91	-2.94	eqw	5.17	0.07
FeI	4175.64	2.85	-0.83	eqw	5.28	0.05
FeI	4181.76	2.83	-0.37	eqw	5.19	0.06
FeI	4182.38	3.02	-1.18	eqw	5.08	0.05
FeI	4184.89	2.83	-0.87	eqw	5.14	0.05
FeI	4187.04	2.45	-0.56	eqw	5.15	0.06
FeI	4187.8	2.42	-0.51	eqw	5.14	0.06
FeI	4191.43	2.47	-0.67	eqw	5.17	0.06
FeI	4195.33	3.33	-0.49	eqw	5.21	0.05
FeI	4199.1	3.05	0.16	eqw	5.07	0.06
FeI	4202.03	1.49	-0.69	eqw	5.18	0.11
FeI	4216.18	0.0	-3.36	eqw	5.36	0.09
FeI	4217.55	3.43	-0.48	eqw	5.22	0.05
FeI	4222.21	2.45	-0.91	eqw	5.09	0.06
FeI	4227.43	3.33	0.27	eqw	5.19	0.05
FeI	4233.6	2.48	-0.6	eqw	5.17	0.06
FeI	4238.81	3.4	-0.23	eqw	5.2	0.05

FeI	4250.12	2.47	-0.38	eqw	5.14	0.06
FeI	4250.79	1.56	-0.71	eqw	5.19	0.1
FeI	4260.47	2.4	0.08	eqw	5.11	0.09
FeI	4271.15	2.45	-0.34	eqw	5.13	0.07
FeI	4271.76	1.49	-0.17	eqw	5.22	0.15
FeI	4282.4	2.18	-0.78	eqw	5.12	0.06
FeI	4325.76	1.61	0.01	eqw	5.11	0.14
FeI	4352.73	2.22	-1.29	eqw	5.22	0.06
FeI	4375.93	0.0	-3.0	eqw	5.23	0.09
FeI	4388.41	3.6	-0.68	eqw	5.21	0.04
FeI	4404.75	1.56	-0.15	eqw	5.21	0.14
FeI	4415.12	1.61	-0.62	eqw	5.19	0.11
FeI	4427.31	0.05	-2.92	eqw	5.25	0.09
FeI	4430.61	2.22	-1.73	eqw	5.16	0.06
FeI	4442.34	2.2	-1.23	eqw	5.24	0.06
FeI	4443.19	2.86	-1.04	eqw	5.08	0.05
FeI	4447.72	2.22	-1.36	eqw	5.23	0.06
FeI	4461.65	0.09	-3.19	eqw	5.28	0.08
FeI	4466.55	2.83	-0.6	eqw	5.15	0.05
FeI	4484.22	3.6	-0.64	eqw	5.04	0.04
FeI	4494.56	2.2	-1.14	eqw	5.21	0.06
FeI	4531.15	1.48	-2.1	eqw	5.19	0.07
FeI	4592.65	1.56	-2.46	eqw	5.36	0.07
FeI	4602.94	1.49	-2.21	eqw	5.28	0.07
FeI	4619.29	3.6	-1.06	eqw	5.07	0.04
FeI	4637.5	3.28	-1.29	eqw	5.12	0.05
FeI	4647.43	2.95	-1.35	eqw	5.21	0.05
FeI	4668.13	3.27	-1.08	eqw	5.17	0.05
FeI	4733.59	1.49	-2.99	eqw	5.37	0.07
FeI	4736.77	3.21	-0.67	eqw	5.14	0.05
FeI	4871.32	2.87	-0.34	eqw	5.07	0.05
FeI	4872.14	2.88	-0.57	eqw	5.05	0.05
FeI	4890.76	2.88	-0.38	eqw	5.12	0.05
FeI	4891.49	2.85	-0.11	eqw	5.11	0.06
FeI	4903.31	2.88	-0.89	eqw	5.11	0.05
FeI	4918.99	2.86	-0.34	eqw	5.14	0.06
FeI	4920.5	2.83	0.07	eqw	5.11	0.07
FeI	4938.81	2.88	-1.08	eqw	5.17	0.05
FeI	4939.69	0.86	-3.25	eqw	5.29	0.07
FeI	4946.39	3.37	-1.11	eqw	5.09	0.05
FeI	4966.09	3.33	-0.79	eqw	5.18	0.05
FeI	5001.86	3.88	-0.01	eqw	5.29	0.04
FeI	5006.12	2.83	-0.62	eqw	5.1	0.05
FeI	5014.94	3.94	-0.18	eqw	5.22	0.04
FeI	5049.82	2.28	-1.36	eqw	5.25	0.06
FeI	5051.63	0.92	-2.76	eqw	5.33	0.07
FeI	5068.77	2.94	-1.04	eqw	5.15	0.05
FeI	5079.74	0.99	-3.24	eqw	5.32	0.07
FeI	5083.34	0.96	-2.84	eqw	5.13	0.07
FeI	5123.72	1.01	-3.06	eqw	5.39	0.07
FeI	5127.36	0.92	-3.25	eqw	5.29	0.07
FeI	5133.69	4.18	0.36	eqw	5.13	0.04
FeI	5150.84	0.99	-3.04	eqw	5.23	0.07
FeI	5171.6	1.49	-1.72	eqw	5.23	0.07
FeI	5191.45	3.04	-0.55	eqw	5.19	0.05
FeI	5192.34	3.0	-0.42	eqw	5.18	0.05
FeI	5194.94	1.56	-2.02	eqw	5.18	0.07
FeI	5215.18	3.27	-0.86	eqw	5.06	0.05
FeI	5216.27	1.61	-2.08	eqw	5.24	0.07
FeI	5232.94	2.94	-0.06	eqw	5.08	0.06
FeI	5266.56	3.0	-0.38	eqw	5.15	0.05
FeI	5281.79	3.04	-0.83	eqw	5.01	0.05

FeI	5283.62	3.24	-0.45	eqw	5.18	0.05
FeI	5324.18	3.21	-0.11	eqw	5.11	0.05
FeI	5339.93	3.27	-0.63	eqw	4.95	0.05
FeI	5341.02	1.61	-1.95	eqw	5.33	0.07
FeI	5364.87	4.45	0.23	eqw	5.16	0.04
FeI	5367.47	4.42	0.44	eqw	5.06	0.04
FeI	5369.96	4.37	0.54	eqw	5.03	0.04
FeI	5371.49	0.96	-1.64	eqw	5.3	0.1
FeI	5383.37	4.31	0.64	eqw	5.1	0.04
FeI	5397.13	0.92	-1.98	eqw	5.31	0.08
FeI	5405.77	0.99	-1.85	eqw	5.32	0.08
FeI	5410.91	4.47	0.4	eqw	5.08	0.04
FeI	5415.2	4.39	0.64	eqw	5.12	0.04
FeI	5429.7	0.96	-1.88	eqw	5.34	0.08
FeI	5434.52	1.01	-2.13	eqw	5.34	0.08
FeI	5497.52	1.01	-2.82	eqw	5.25	0.07
FeI	5501.47	0.96	-3.05	eqw	5.38	0.07
FeI	5506.78	0.99	-2.79	eqw	5.33	0.07
FeI	5569.62	3.42	-0.52	eqw	5.12	0.05
FeI	5586.76	3.37	-0.11	eqw	5.08	0.05
FeI	5624.54	3.42	-0.76	eqw	5.08	0.05
FeI	5662.52	4.18	-0.41	eqw	5.04	0.04
FeI	6003.01	3.88	-1.1	eqw	5.35	0.04
FeI	6136.61	2.45	-1.41	eqw	5.28	0.06
FeI	6137.69	2.59	-1.35	eqw	5.14	0.06
FeI	6191.56	2.43	-1.42	eqw	5.15	0.06
FeI	6230.72	2.56	-1.28	eqw	5.27	0.06
FeI	6246.32	3.6	-0.77	eqw	5.2	0.05
FeI	6252.56	2.4	-1.77	eqw	5.24	0.06
FeI	6393.6	2.43	-1.58	eqw	5.28	0.06
FeI	6411.65	3.65	-0.59	eqw	5.2	0.05
FeI	6421.35	2.28	-2.01	eqw	5.34	0.06
FeI	6430.85	2.18	-1.95	eqw	5.28	0.06
FeI	6494.98	2.4	-1.24	eqw	5.23	0.06
FeI	6677.99	2.69	-1.42	eqw	5.31	0.06
FeI	7495.07	4.22	-0.1	eqw	5.23	0.04
FeII	2424.39	2.58	-0.94	syn	5.2	0.04
FeII	2428.8	3.89	-0.31	syn	5.0	0.07
FeII	2434.24	5.29	0.25	syn	5.0	0.08
FeII	2437.65	5.2	-0.36	syn	5.1	0.08
FeII	2439.3	3.15	0.45	syn	4.88	0.08
FeII	2444.51	2.58	0.3	syn	5.2	0.06
FeII	2445.57	2.7	0.05	syn	4.84	0.08
FeII	2458.97	3.89	-0.04	syn	4.9	0.08
FeII	2461.28	3.23	0.23	syn	5.12	0.08
FeII	2461.86	3.22	0.34	syn	4.95	0.08
FeII	2463.28	3.15	-0.19	syn	5.11	0.1
FeII	2465.91	3.22	-0.05	syn	5.1	0.08
FeII	2472.61	5.55	0.47	syn	5.2	0.08
FeII	2503.87	3.77	0.32	syn	5.19	0.12
FeII	2572.97	2.89	-1.2	syn	5.3	0.09
FeII	2587.95	4.15	0.23	syn	5.15	0.07
FeII	2664.66	3.39	0.31	syn	5.15	0.08
FeII	2718.64	6.22	0.02	syn	5.15	0.06
FeII	2892.83	1.08	-2.7	syn	5.2	0.03
FeII	2944.39	1.7	-0.85	syn	5.24	0.09
FeII	2984.82	1.67	-0.45	syn	5.15	0.08
FeII	2985.55	1.72	-0.89	syn	5.12	0.07
FeII	4173.45	2.58	-2.38	eqw	5.28	0.03
FeII	4178.86	2.58	-2.51	eqw	5.2	0.03
FeII	4233.16	2.58	-2.02	eqw	5.26	0.04
FeII	4385.38	2.78	-2.64	eqw	5.2	0.03

FeII	4416.82	2.78	-2.57	eqw	5.14	0.03
FeII	4491.41	2.86	-2.71	eqw	5.17	0.03
FeII	4508.28	2.86	-2.42	eqw	5.29	0.03
FeII	4515.34	2.84	-2.6	eqw	5.35	0.03
FeII	4555.89	2.83	-2.4	eqw	5.23	0.03
FeII	4576.34	2.84	-2.95	eqw	5.22	0.03
FeII	4583.83	2.81	-1.94	eqw	5.26	0.03
FeII	5197.58	3.23	-2.22	eqw	5.23	0.03
FeII	5234.63	3.22	-2.18	eqw	5.19	0.03
FeII	5276.0	3.2	-2.01	eqw	5.2	0.03
CoI	2316.85	0.17	-1.15	syn	2.95	0.14
CoI	3405.12	0.43	0.29	syn	2.98	0.09
CoI	3409.18	0.51	-0.22	syn	2.76	0.1
CoI	3433.04	0.63	-0.18	syn	2.84	0.08
CoI	3449.17	0.58	-0.12	syn	2.75	0.1
CoI	3449.44	0.43	-0.48	syn	2.87	0.09
CoI	3489.4	0.92	0.18	syn	2.64	0.05
CoI	3513.48	0.1	-0.79	syn	3.09	0.07
CoI	3529.03	0.17	-0.89	syn	2.96	0.08
CoI	3995.31	0.92	-0.18	syn	2.87	0.05
CoI	4121.32	0.92	-0.33	syn	2.94	0.06
CoII	2311.6	0.56	0.32	syn	2.55	0.1
CoII	2326.14	0.57	-0.42	syn	2.7	0.03
CoII	2330.36	0.61	-0.51	syn	2.8	0.06
CoII	2361.52	0.64	-1.16	syn	2.65	0.13
CoII	2393.91	0.57	-0.37	syn	2.6	0.12
CoII	2414.07	0.57	-0.37	syn	2.6	0.06
CoII	2417.66	0.5	-0.25	syn	2.49	0.09
CoII	2464.2	1.22	-0.4	syn	2.57	0.35
CoII	2564.0	1.33	0.03	syn	2.55	0.0
NiI	2441.82	0.21	-1.51	syn	3.95	0.07
NiI	2984.13	0.0	-1.5	syn	3.8	0.13
NiI	2992.59	0.02	-1.22	syn	4.0	0.1
NiI	3423.71	0.21	-0.71	eqw	4.0	0.16
NiI	3433.56	0.03	-0.67	eqw	3.96	0.17
NiI	3437.28	0.0	-1.2	eqw	3.93	0.13
NiI	3452.89	0.11	-0.9	eqw	4.34	0.18
NiI	3472.54	0.11	-0.79	eqw	3.8	0.14
NiI	3483.78	0.27	-1.11	eqw	3.75	0.1
NiI	3492.96	0.11	-0.24	eqw	4.0	0.19
NiI	3500.85	0.17	-1.27	eqw	4.1	0.12
NiI	3524.54	0.03	0.01	eqw	4.01	0.19
NiI	3566.37	0.42	-0.24	eqw	3.83	0.17
NiI	3597.7	0.21	-1.1	eqw	4.08	0.14
NiI	3783.53	0.42	-1.4	eqw	3.97	0.08
NiI	3807.14	0.42	-1.23	eqw	3.92	0.09
NiI	4604.99	3.48	-0.24	eqw	4.02	0.04
NiI	4648.65	3.42	-0.09	eqw	3.88	0.04
NiI	4714.42	3.38	0.25	eqw	3.94	0.04
NiI	5080.53	3.65	0.32	eqw	3.56	0.04
NiI	5476.9	1.83	-0.78	eqw	3.9	0.06
NiII	2297.49	1.32	-0.33	syn	3.98	0.18
NiII	2350.85	1.68	-2.28	syn	3.92	0.17
NiII	2356.40	1.86	-0.83	syn	3.91	0.07
NiII	2415.0	1.86	0.13	syn	4.0	0.0
NiII	2437.0	1.68	-0.33	syn	3.91	0.04
ZnI	4722.15	4.03	-0.37	syn	2.31	0.04
ZnI	4810.53	4.08	-0.15	syn	2.33	0.04
GeI	3039.07	0.88	-0.07	syn	1.4	0.17
AsI	2288.11	1.35	-0.06	syn	<0.84	-
RbI	7947.6	0.0	-0.16	syn	<2.42	-
SrII	4077.71	0.0	0.15	syn	1.01	0.18

SrII	4215.52	0.0	-0.17	syn	1.1	0.18
YII	2422.19	0.41	-0.08	syn	0.58	0.06
YII	3549.0	0.13	-0.29	syn	0.47	0.06
YII	3600.73	0.18	0.34	syn	0.6	0.08
YII	3611.04	0.13	0.05	syn	0.28	0.05
YII	3950.35	0.1	-0.73	syn	0.5	0.05
YII	3982.59	0.13	-0.56	syn	0.43	0.06
YII	4235.73	0.13	-1.27	syn	0.65	0.03
YII	4398.01	0.13	-0.75	syn	0.45	0.07
YII	4883.68	1.08	0.19	syn	0.24	0.04
YII	5205.72	1.03	-0.28	syn	0.55	0.06
ZrII	2567.64	0.0	-0.17	syn	0.99	0.04
ZrII	2700.13	0.1	-0.08	syn	1.05	0.0
ZrII	2745.85	0.10	-0.31	syn	1.19	0.02
ZrII	2758.81	0.0	-0.56	syn	1.12	0.22
ZrII	2915.99	0.47	-0.5	syn	1.12	0.1
ZrII	3430.53	0.47	-0.16	syn	1.15	0.0
ZrII	3505.67	0.16	-0.39	syn	1.2	0.05
ZrII	3551.95	0.1	-0.36	syn	1.24	0.07
ZrII	3998.96	0.56	-0.52	syn	1.1	0.05
ZrII	4149.2	0.8	-0.04	syn	1.07	0.05
ZrII	4156.23	0.71	-0.78	syn	1.0	0.06
ZrII	4161.2	0.71	-0.59	syn	1.2	0.06
ZrII	4208.98	0.71	-0.51	syn	1.15	0.05
ZrII	4359.73	1.24	-0.51	syn	1.25	0.09
ZrII	4496.96	0.71	-0.89	syn	1.19	0.05
NbII	2927.81	0.51	0.16	syn	<0.93	–
MoII	2871.51	1.54	0.06	syn	0.75	0.05
RuII	2456.0	1.35	0.06	syn	<1.54	–
RhI	3434.89	0.0	0.44	syn	<1.52	–
PdI	3404.58	0.81	0.32	syn	<1.34	–
AgI	3382.89	0.0	-0.33	syn	<1.38	–
CdI	2288.02	0.0	0.11	syn	0.63	0.13
InII	2306.06	0.0	-2.3	syn	<0.83	–
SnI	2286.68	0.42	-0.94	syn	<2.94	–
Tel	2385.79	0.59	-0.81	syn	<1.83	–
BaII	4554.03	0.0	0.17	syn	0.55	0.07
BaII	4934.08	0.0	-0.16	syn	0.4	0.07
BaII	5853.68	0.6	-0.91	syn	0.47	0.03
BaII	6141.71	0.7	-0.08	syn	0.5	0.06
BaII	6496.9	0.6	-0.38	syn	0.47	0.04
LaII	3949.1	0.4	0.49	syn	-0.2	0.06
LaII	3988.51	0.4	0.21	syn	-0.2	0.06
LaII	4077.34	0.24	-0.06	syn	-0.05	0.07
LaII	4086.71	0.0	-0.07	syn	-0.18	0.05
LaII	4123.22	0.32	0.13	syn	-0.16	0.06
CeII	4460.21	0.48	0.28	syn	0.22	0.02
CeII	4562.36	0.48	0.21	syn	0.25	0.07
PrII	4225.32	0.0	0.32	syn	-0.4	0.2
NdII	3900.22	0.47	0.1	syn	0.3	0.12
NdII	4012.24	0.63	0.81	syn	0.07	0.19
NdII	4109.45	0.32	0.35	syn	0.03	0.07
NdII	4156.08	0.18	0.16	syn	0.1	0.07
NdII	4177.32	0.06	-0.1	syn	0.34	0.09
NdII	4303.57	0.0	0.08	syn	0.17	0.13
SmII	4329.02	0.18	-0.51	syn	0.18	0.07
EuII	3819.67	0.0	0.51	syn	-0.51	0.04
EuII	3907.11	0.21	0.17	syn	-0.41	0.04
EuII	4129.72	0.0	0.22	syn	-0.47	0.03
EuII	4205.04	0.0	0.21	syn	-0.44	0.04
EuII	4435.58	0.21	-0.11	syn	-0.45	0.11
GdII	3032.84	0.08	0.3	syn	0.4	0.19

GdII	4063.38	0.99	0.33	syn	0.4	0.18
GdII	4251.73	0.38	-0.22	syn	0.35	0.07
TbII	3874.17	0.0	0.27	syn	<-0.06	-
DyII	3407.8	0.0	0.18	syn	0.3	0.09
DyII	3531.71	0.0	0.77	syn	0.32	0.19
DyII	3757.37	0.1	-0.17	syn	0.37	0.06
DyII	3944.68	0.0	0.11	syn	0.17	0.04
DyII	4077.97	0.1	-0.04	syn	0.15	0.05
HoII	3456.01	0.0	0.76	syn	-0.42	0.07
HoII	4045.45	0.0	-0.05	syn	-0.3	0.07
ErII	3499.1	0.06	0.29	syn	0.22	0.07
ErII	3906.31	0.0	0.12	syn	0.01	0.12
TmII	3848.02	0.0	-0.14	syn	-0.67	0.06
YbII	3694.19	0.0	-0.3	syn	-0.27	0.05
LuII	2615.41	0.0	0.11	syn	-0.7	0.17
HfII	3399.79	0.0	-0.57	syn	<0.67	-
OsII	2282.28	0.0	-0.57	syn	0.49	0.29
IrI	2639.71	0.0	-0.31	syn	<1.01	-
PtI	2659.45	0.0	-0.03	syn	0.53	0.1
PtI	2997.96	0.10	-0.50	syn	0.68	0.16
AuI	2427.95	0.0	-0.15	syn	-0.1	0.12
AuI	2675.95	0.0	-0.45	syn	-0.02	0.11
ThII	4019.13	0.0	-0.23	syn	<-0.38	-
UII	3859.57	0.04	-0.07	syn	<0.43	-
C-H	4313.0	-	-	syn	6.7	0.12
C-N	3875.0	-	-	syn	<7.73	-

Table A1: Wavelength, excitation potential, and oscillator strength of all absorption lines used are listed. Also listed is the abundance determination technique used i.e., spectral synthesis (syn) or EW measurement (ew). In the final columns, the abundance of the line and the associated systematic uncertainty are listed.

This paper has been typeset from a  $\text{\TeX}/\text{\LaTeX}$  file prepared by the author.